

FACILITY FORM 802

N65-24293

(ACCESSION NUMBER)

60

(PAGES)

CB-62810

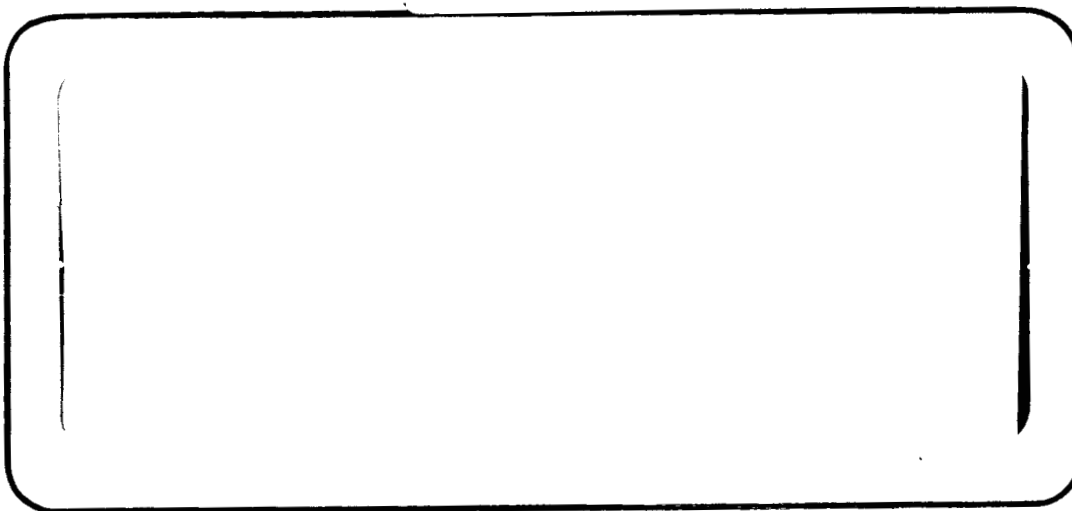
(NASA CR OR TMX OR AD NUMBER)

(THRU)

(CODE)

32

(CATEGORY)



GPO PRICE \$ _____

OTS PRICE(S) \$ _____

Hard copy (HC) \$3.00

Microfiche (MF) 100

TRW SPACE TECHNOLOGY LABORATORIES

THOMPSON RAMO WOOLDRIDGE INC.

ONE SPACE PARK • REDONDO BEACH, CALIFORNIA

11

4 February 1965

Final Technical Report

"STUDY OF MICROMETEOROID DAMAGE TO
THERMAL CONTROL MATERIALS"

Prepared for:

National Aeronautics and Space Administration
George C. Marshall Space Flight Center
Huntsville, Alabama 35812

Contract No. NAS8-11149

J. F. Friichtenicht

Prepared by
J. F. Friichtenicht

Bernard Hamermond

Approved by (for)
D. B. Langmuir
Director

PHYSICAL ELECTRONICS LABORATORY
Physical Research Division
TRW Space Technology Laboratories
Thompson Ramo Wooldridge Inc.
One Space Park, Redondo Beach, California

TABLE OF CONTENTS

	Page
List of Figures.	iii
List of Tables	v
I. Introduction	1
II. Experimental Apparatus and Procedures.	3
A. Target Bombardment Phase.	3
1. The Electrostatic Accelerator.	3
2. Particle Parameter Analysis.	6
3. Target Bombardment Apparatus	15
B. Radiation Measurement Phase	18
C. Target Damage Assessment.	29
III. Experimental Results	36
A. Emissivity Measurements	36
B. Specular Reflectance Measurements	45
C. Hypervelocity Cratering	47
IV. Discussion of Results.	51
V. Summary.	54
References	55

LIST OF FIGURES

Figure	Caption	Page
1	Block Diagram of the Automatic Particle Injector Pulser.	5
2	Sampling of Particle Parameters Obtained Using the Semi-Automatic Analyzing System. . .	9
3	Functional Block Diagram of Automatic Particle Parameter Analysis System	11
4	Example of Particle Parameter Analysis Using the X-Y Plotter. The equal R curves were generated from $R^3 = 5 \times y^2$. The data points were transferred from a photographic record of a typical run. The actual particle radius in microns represented by each R curve is noted at the left-hand terminus of each equal R curve.	14
5	Schematic Diagram of the Target Bombardment System	16
6	Over-all View of the Target Bombardment Apparatus.	19
7	Exterior View of the Target Bombardment Chamber.	20
8	Interior View of the Target Bombardment Chamber.	21
9	The Gier-Dunkle Integrating Sphere Absolute Reflectometer.	23
10	The Gier-Dunkle Heated Cavity Absolute Reflectometer.	24
11	The Goniometric Bi-directional Reflectometer .	26
12	Schematic Diagram of the Goniometric Bi-directional Reflectometer	27
13	Photographs of Gold Targets. The upper and lower photographs were taken after bombardment by 100,000 and 400,000 impacts, respectively. Magnification is 500X in both cases.	30

LIST OF FIGURES CONTINUED

14	Photographs of Two Stainless Steel Targets After Bombardment by 300,000 Particles (upper) and 600,000 Particles (lower). Magnification is 1000X.	31
15	Photographs of Vacuum Deposited Aluminum After Particle Bombardment. The upper photo followed bombardment by 300,000 particles while the lower was taken after 600,000 impacts. Magnification is 1000X . . .	32
16	Histogram of Crater Diameters for a Gold Target. (Sample 47-64)	33
17	Histogram of Crater Diameters for a Stainless Steel Target. (Sample 51-64)	34
18	Spectral Reflectance of a Gold Sample Before and After Particle Bombardment	37
19	Spectral Reflectance of a Gold Sample Before and After Particle Bombardment. The bombardment was done in two steps as shown. . . .	38
20	Spectral Reflectance of a 304 Stainless Steel Sample Before and After Particle Bombardment.	39
21	Spectral Reflectance of a 304 Stainless Steel Sample Before and After Particle Bombardment.	40
22	Spectral Reflectance of a Vacuum Deposited Aluminum Sample Before and After Particle Bombardment.	41
23	Spectral Reflectance of a Vacuum Deposited Aluminum Sample Before and After Particle Bombardment.	42
24	Histogram of Particle Radii. The data were obtained with the electronic X-Y plotter over several different runs.	48
25	Electron Micrograph of the Iron Particles (Magnification 30,000X). The scale divisions correspond to one micron	50

LIST OF TABLES

Table		Page
I.	Effect of Simulated Micrometeorite Bombardment upon Integrated Directional Reflectance.	44
II	Effect of Simulated Micrometeorite Bombardment upon the Specular Reflectance. .	46
III	Calculated Crater Coverage for Natural Meteoroids	53

STUDY OF MICROMETEOROID DAMAGE TO THERMAL CONTROL MATERIALS

I. INTRODUCTION

This report summarizes the work performed under NASA Contract NAS8-11149, for the period from 7 February 1964 to 3 November 1964. The objective of the program was to study experimentally the effects of micrometeoroid damage on metallic thermal control materials.

As space exploration programs become more ambitious, the hazard posed to successful spacecraft performance by the continual meteoroid bombardment to which it is exposed, becomes increasingly significant. In the past, emphasis was placed on the problem of catastrophic damage as the result of chance collisions with relatively large meteoroids. However, more frequent encounters are made with less damaging micrometeoroids which are known to exist in much greater numbers. Such collisions can reduce spacecraft performance by gradually producing changes in the surface properties of materials. Thermal control systems of spacecraft depend, to some extent, upon the properties of passive thermal radiators. Significant changes in these properties could alter the temperature balance which, in turn, could jeopardize the mission.

It is generally assumed that micrometeoroid damage will cause a change in thermal radiative properties by erosion of thermal control coatings or by roughening of metallic surfaces. For the latter case, pitting of a metallic surface by micrometeoroid bombardment will likely result in increased emittance. Second order effects, such as work hardening, could also contribute to change. At the present time, neither the micrometeoroid flux nor the effects of meteoritic impact are known

well enough to predict, in advance, the over-all effect of exposure to the space environment. Accordingly, this program was undertaken at TRW Space Technology Laboratories to provide additional information on the effects of micrometeoroid bombardment.

Simply stated, the experimental program consisted of measuring the emissivity of highly reflecting metallic materials before and after subjecting the test samples to varying degrees of simulated micrometeoroid exposure. The observed changes were then correlated to surface damage in terms of the fractional area covered by craters and the total number of impacting particles. From these data, the magnitude of the anticipated change in the actual space environment can be determined providing the meteoroid flux is known. Furthermore, the relative susceptibility to change of various materials can be deduced from the data. At first sight, the observed effects appear to be relatively small. However, the end result depends, to a great extent, upon the numbers and properties of the natural meteoroid environment.

Although the experiments are relatively straightforward, a certain amount of care was exercised in data acquisition and analysis in order to achieve maximum benefit from the program. Experimental apparatus and procedures are discussed in the following section. The experimental results are presented in Section III, while the conclusions drawn from these results are discussed in Section IV.

II. EXPERIMENTAL APPARATUS AND PROCEDURES

A. Target Bombardment Phase

1. The Electrostatic Accelerator

The STL electrostatic hypervelocity accelerator¹ was used as a source of high-speed particles for all of the measurements described here. In this accelerator, small particles are charged electrically by a process described elsewhere², and are injected into the accelerating field of a 2-million volt Van de Graaff generator. They are subsequently accelerated to a final velocity given by $v = (2qV/m)^{1/2}$, where V is the accelerating voltage, m the mass of the particle, and q its charge. As described in Ref. 2, the q/m ratio is proportional to the reciprocal of particle radius. Consequently, the electrostatic method of accelerating particles is most effective for small particles. Under optimum conditions, a one-micron diameter iron particle achieves a final velocity of nearly 8 km/sec. Higher q/m ratios and correspondingly higher velocities are achieved with lower density materials and smaller particles. Velocities up to 30 km/sec have been observed with smaller iron particles and also with carbon particles. For the work described here, only iron particles with a mean diameter of about 1.5 microns were used. Considerably smaller particles were present in the sample, but no attempt to detect them was made because their contribution to surface damage was considered to be negligible.

The charge and velocity of particles from the accelerator are determined by measuring the magnitude and duration, respectively, of a voltage signal induced on a cylindrical drift tube of known capacitance and length through which the particle passes. The charge is given by $q = CV_i$,

where V_i is the amplitude of the pulse and C is the capacitance of the drift tube to ground. The velocity is simply $v = \ell/t$, where t is the transit time through a cylinder of length ℓ . The mass (hence, the radius) of the particle is found from $m = 2qV/v^2$. Usually, the signal is amplified and displayed on an oscilloscope trace which is photographed for later analysis.

The manual operation of the charged particle injector, utilized before this program was begun, is not applicable to experiments where high repetition rates are required. Accordingly, an automatic particle injector control system was installed in the accelerator. The injector and associated components are located within the high voltage terminal of the Van de Graaff. Control of the unit is accomplished by means of selsyn- and solenoid-driven control rods which extend the length of the accelerator column and are operated from the control console.

In order to expel particles from the injector, it is necessary to provide a 10 to 15 kv pulse of about 10 milliseconds duration to the injector. In the manual mode, a pulse was generated by discharging a capacitor through a pulse forming network. The pulse was fed to a high voltage pulse tube whose output was applied to the injector. The sequence of events was initiated by actuation of one of the solenoid-driven control rods.

In the automatic mode (illustrated in Fig. 1), the trigger pulses are obtained from a free running multivibrator. The multivibrator repetition rate is adjustable to five different values by selection of the coupling capacitors which are mounted on two six-position wafer switches. Switching of the capacitors is accomplished by means of a solenoid-driven stepping switch. Each time the solenoid is actuated, the wafer

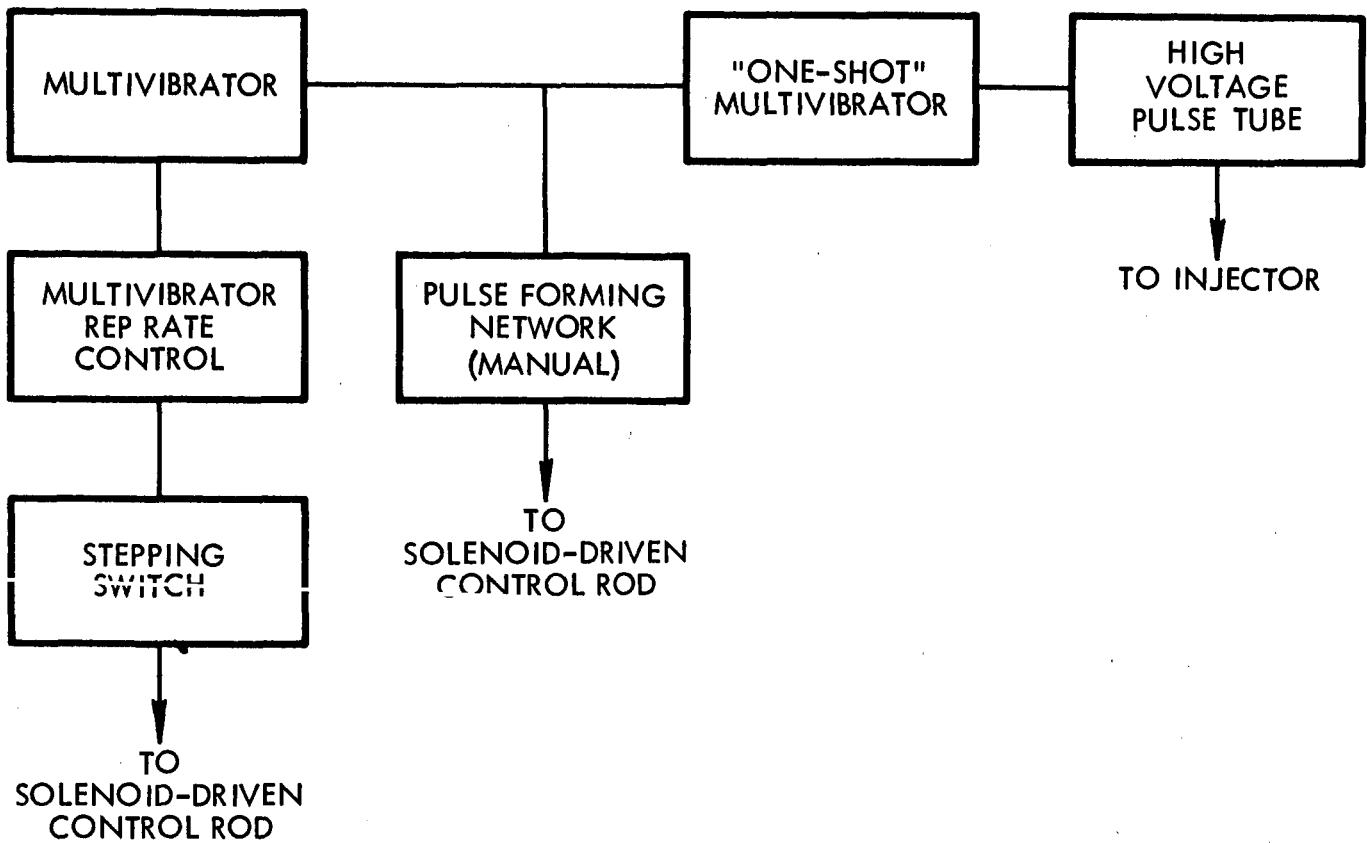


Figure 1. Block Diagram of the Automatic Particle Injector Pulser.

switch is advanced one position. A similar wafer switch, located within the control console, controls lamps which indicate the position of the switch at any time.

The repetition rates available are 10, 30, 100, 300, and 600 per minute and manual. In the manual position, the multivibrator is turned off and the injector is triggered manually as before.

Trigger signals derived from either the multivibrator or the manual pulse forming network are fed to a "one-shot" multivibrator which supplies a square wave signal to the grid of the high voltage pulse tube. The duration of this signal is set at about 10 milliseconds. The amplitude of the input signal determines the amplitude of the output voltage pulse and is adjustable from the control console.

The number of particles injected per pulse is a function of pulse amplitude and duration. Normally, these quantities are adjusted to give one particle per pulse on the average. The particle impact rate for most of the work was set at 600 per minute (10/sec). During the latter part of the program, the impact rate was successfully raised to about 20/sec by increasing the amplitude of the injection pulse.

2. Particle Parameter Analysis

In order to apply the results of laboratory experiments to the problems of the actual space environment, the parameters of the particles used in the experiments must be determined. However, it is not necessary to measure the parameters of all of the particles because only the combined effects of many particle impacts are significant. A more reasonable approach is to count the total number of particles incident on the target sample and to analyze a sufficient number of them to

specify the distribution of particle masses and velocities. Two data analyzing systems, both incorporating the sampling concept, were used in this program.

The counting system for recording the total number of particle impacts was common to both systems. Detector signals, in the form of rectangular voltage pulses, were fed to a voltage discriminator. Signals with amplitudes exceeding the discrimination level produce a standard voltage pulse. These are presented to a Baird-Atomic decade scaler which is conventional in all respects. In operation, the discrimination level was set comfortably above the noise level. Furthermore, the discriminator would reject low frequency noise even if it exceeded the voltage threshold. As mentioned earlier, no special effort was made to record the very small, fast particles which contribute negligible damage to the target surface.

In one method of data analysis, the detector signals were displayed on an oscilloscope and photographed for later analysis. In order to obtain random samples of detector signals, the camera shutter was actuated by a camera controller unit. This unit consists of a number of clock relays which controlled the exposure time and the interval between exposures.

In order to minimize confusion which arises from multiple detector signals on a single frame, the oscilloscope was operated in the single sweep mode. This was accomplished by paralleling the manual reset switch on the oscilloscope by the camera flash contacts. When these contacts were closed, the oscilloscope was armed and the next detector signal to come along triggered the oscilloscope sweep. No more signals were displayed until the cycle of camera operation was repeated.

Random samples were obtained by ensuring that no time correlation existed between the injection of particles and

actuation of the camera shutter. Usually, the exposure interval was set at one minute which meant that about 500 traces would be recorded in one day's running time.

To reduce the data acquired in this method, the signal amplitude and duration are read from the photographs by means of a Telereader*. The information is punched onto computer cards by an IBM key punch machine which is used in conjunction with the Telereader. These cards, along with cards carrying the values of the other system variables, are fed to an IBM-7094 computer which performs the calculations. The results are retrieved from the computer in printed form. Graphical representation of typical data analyzed in this manner is illustrated in Fig. 2.

The method of data analysis described above, although considerably faster than manual data acquisition and analysis, still leaves something to be desired. Another system which automatically displays the data in graphical form was used during the latter part of the program. The main component of this system is an electronic X-Y plotter which had been developed under another contract (NAS3-5755), but was available for use on this program.

In this system, each particle is represented by a point on a two-dimensional display. The displacement of the point along the Y axis is proportional to particle charge and the displacement in the X direction is proportional to the transit time through the detector. Each point represents a unique velocity and mass. Since each particle is represented by a single point, in contrast to a rectangular pulse in the former method, a large number of data points can be placed on a single display before confusion arises. As will be shown

*Manufactured by Telecomputing Corporation.

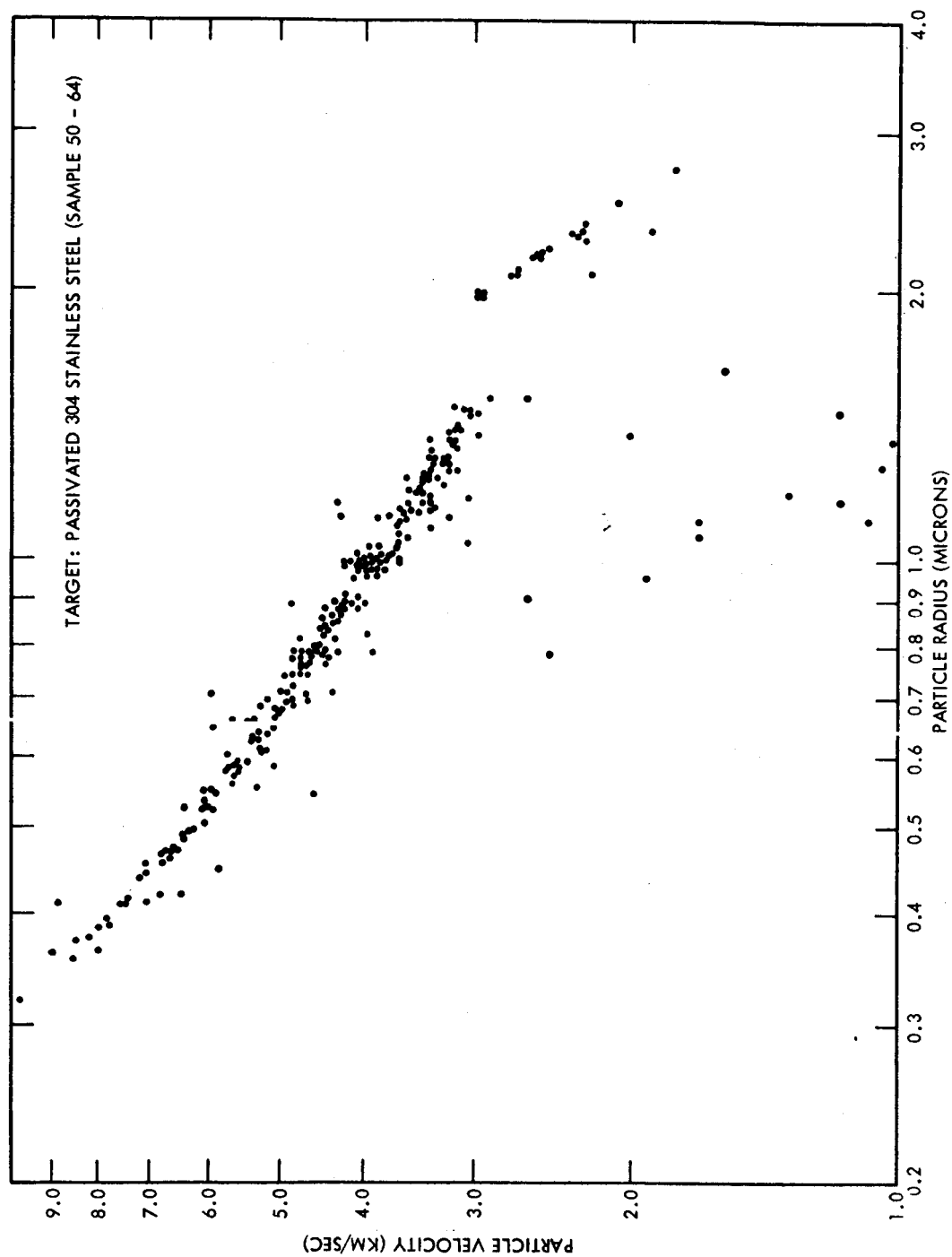


Figure 2. Sampling of Particle Parameters Obtained Using the Semi-Automatic Analyzing System.

later, lines of constant radius and velocity can be drawn on the plot. The lines form a number of irregularly shaped areas. Each of the areas corresponds to a specific velocity and radius range. The radius and velocity of each particle can be determined to fairly good accuracy by simply observing into which area the point falls.

A simplified block diagram of the circuit is shown in Fig. 3. The pulse from the particle detector is fed to three separate circuits. In the pulse stretcher, a pulse is generated with the same amplitude as the input pulse, but much longer. The stretched pulse is applied to the vertical amplifier of an oscilloscope and deflects the beam vertically by an amount equal to the original pulse height. The oscilloscope sweep is triggered when the detector pulse exceeds the threshold imposed by the discriminator. Finally, the detector pulse is fed to a differentiating network. The resulting negative spike, which occurs at the trailing edge of the detector pulse, is fed to the oscilloscope brightener pulse generator. This unit, in turn, delivers a short duration, rectangular voltage pulse to the cathode of the oscilloscope. In operation, the beam intensity control of the oscilloscope is adjusted so that the trace is visible only when the brightening pulse is applied to the cathode. Since brightening occurs at the trailing edge of the pulse and, at the same time, the vertical displacement is proportional to detector pulse height, the position of the brightened spot gives the desired information.

The amplitude of a detector signal (or the displacement of a point along the Y axis when using the X-Y plotter) is given by

$$V_o = \frac{qG}{C} \quad (1)$$

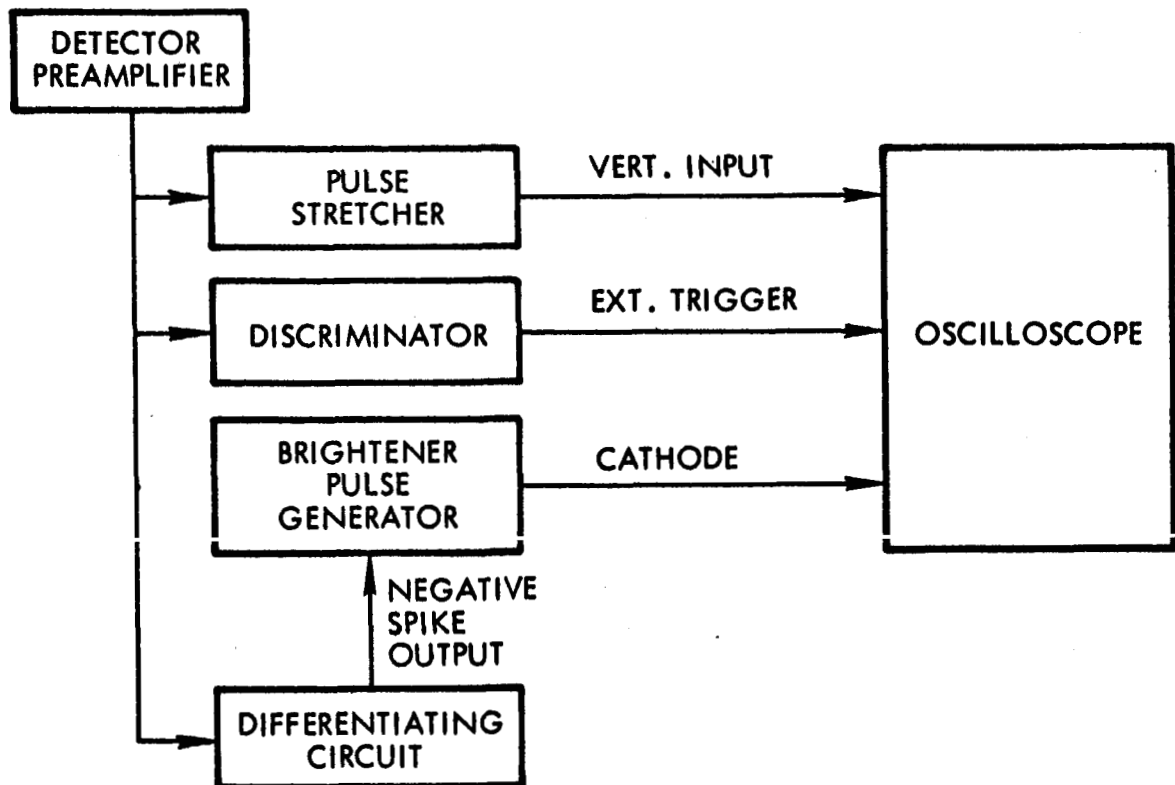


Figure 3. Functional Block Diagram of Automatic Particle Parameter Analysis System.

where V_o is the signal amplitude in volts, q the particle charge, C the capacitance of the detector and G the voltage gain of the preamplifier. Defining $V_o = yS_v$, where y is the amplitude in scale divisions and S_v is the sensitivity of the oscilloscope in volts/scale division, we get

$$q = y \left(\frac{S_v C}{G} \right) \quad (2)$$

Similarly, the duration of the signal (or X displacement) is the transit time τ through a detector of known length ℓ . From this we get

$$v = \frac{\ell}{\tau} = \frac{\ell}{xS_s} \quad (3)$$

where x is the signal length in scale divisions and S_s is the sweep sensitivity in seconds/scale division. Substituting into the conservation of energy equation

$$\frac{mv^2}{2} = qV \quad (4)$$

where m is particle mass and V the accelerating voltage, and rearranging, we get

$$m = \left(\frac{2 S_v S_s^2 CV}{G \ell^2} \right) yx^2 \quad (5)$$

For spherical particles of density ρ , the radius r is obtained from

$$r^3 = \left(\frac{3 S_v S_s^2 CV}{2\pi\rho G \ell^2} \right) yx^2 \quad (6)$$

For any given experiment, the quantities in brackets are constant and are known. Thus, we can write

$$\frac{r^3}{K} = yx^2 \quad . \quad (7)$$

Given the X and Y displacements of a given point and specifying a value for K, the radius of the particle represented by the point is determined uniquely. Furthermore, lines of equal radius can be specified by plotting curves of $yx^2 = \text{constant}$.

To avoid the problem of generating and plotting new sets of curves each time K is changed, we introduce two new quantities; namely, R a parametric radius and K_1 an arbitrary constant such that

$$\frac{R^3}{K_1} = yx^2 \quad . \quad (8)$$

Choosing an arbitrary value of K_1 , and letting R take on different values, a family of equal R curves may be plotted.

From Eqs. (7) and (8), we see that

$$\frac{R^3}{K_1} = \frac{r^3}{K} \quad \text{or} \quad r = \left(\frac{K}{K_1} \right)^{1/3} R \quad . \quad (9)$$

The curves generated for R are universal. Once a specified value for K is determined, the equal R curves may be relabeled by use of Eq. (9).

This is illustrated in Fig. 4. First, a set of equal R curves with R taking values from 1 through 8 and for $K_1 = 5$ were plotted on the same graph. For this run $K = 2.84 \times 10^{-20}$. Using Eq. (9), we get $r = (0.178)R$ micron. The appropriate labels are shown in the figure.

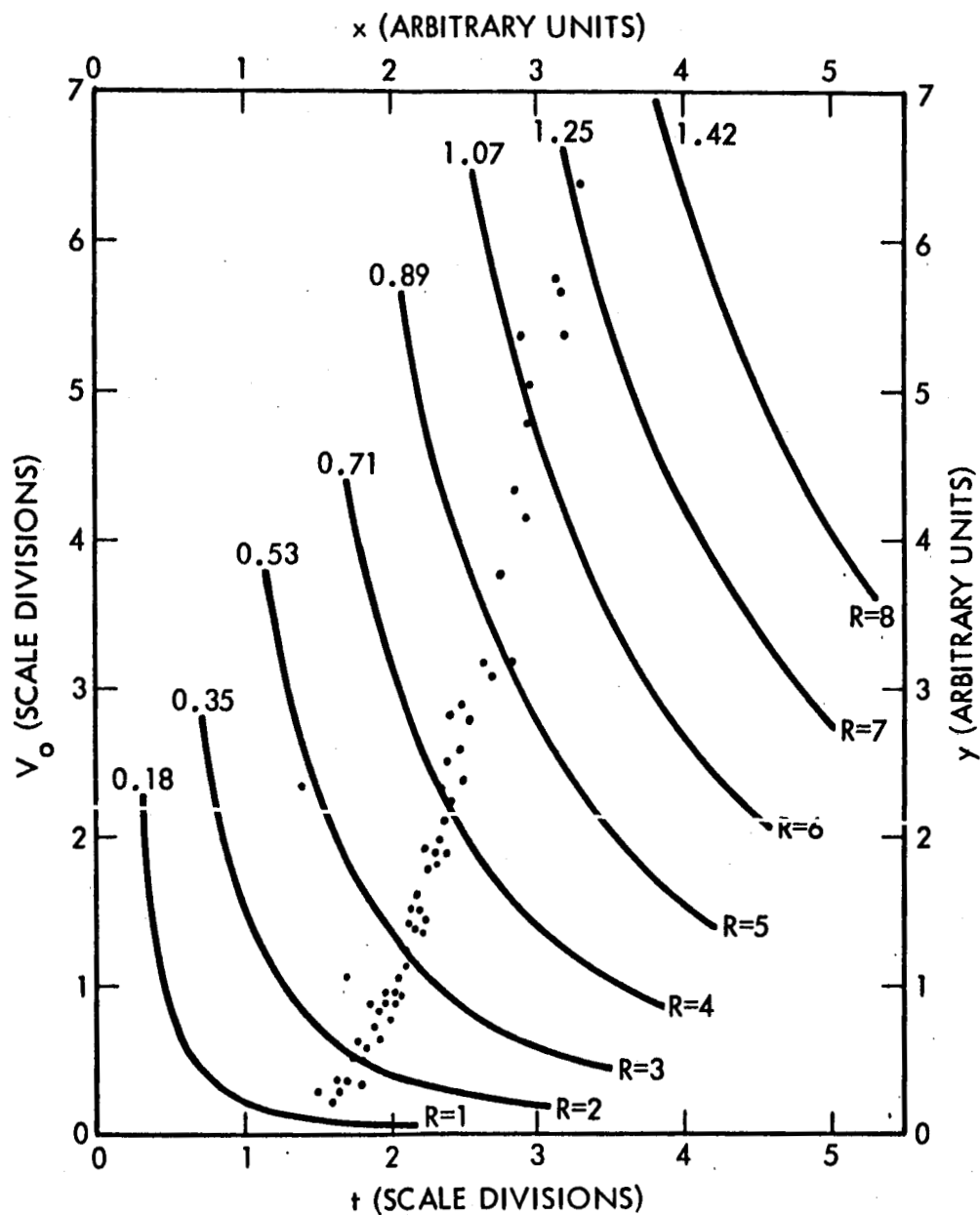


Figure 4. Example of Particle Parameter Analysis Using the X-Y Plotter. The Equal R Curves were generated from $R^3 = 5 \times y^2$. The data points were transferred from a photographic record of a typical run. The actual particle radius in microns represented by each R curve is noted at the left-hand terminus of each R curve.

It should be recognized, also, that the τ axis is proportional to reciprocal velocity. Thus, the velocity and radius of a particular particle can be determined to some degree of accuracy by inspection. The radius of a particular particle can be determined more accurately by interpolation along a line from the origin to the point. Such a line has the form $y = Cx$. Substitution into Eq. (7) yields $r = (CK)^{1/3} x$. Thus, measurement of the slope C and the x displacement yields r precisely.

An oscilloscope graticule, with equal R curves etched on it, was prepared. With this, the data may be read directly from the photograph and the necessity of transposing data points is eliminated.

3. Target Bombardment Apparatus

A block diagram of the target bombardment system is shown in Fig. 5. The target sample is located within a target chamber at the end of the accelerator drift tube. The chamber is mounted on a portable vacuum system which allows rapid coupling and de-coupling of the experiment from the accelerator. The auxiliary vacuum system also provides a better vacuum, which reduces the likelihood of contamination of the sample surface.

Particles from the accelerator first pass through a magnetic deflection system (not shown on the diagram). The function of the magnetic field is to deflect ions from the particle beam in order to minimize the effects of ion bombardment on the sample surface. The magnetic field does not alter the particle trajectory significantly because of the relatively low q/m of the particles.

The undeflected particles pass through a position indicating particle detector which is used primarily for

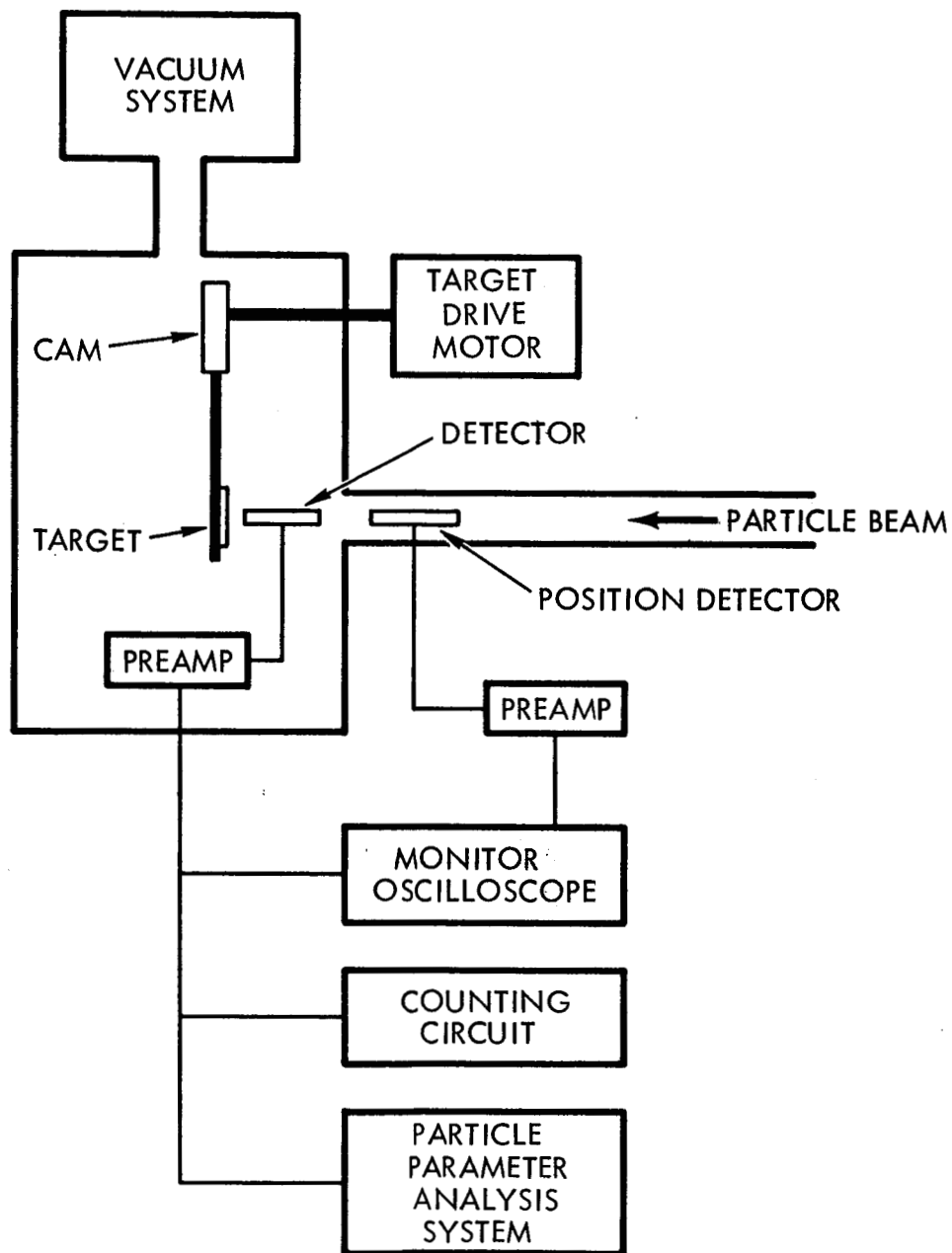


Figure 5. Schematic Diagram of the Target Bombardment System.

focusing and alignment purposes. The particles then pass along the axis of a second detector and impact upon the target surface. Signals from the second detector are processed to obtain particle parameters and to record the number of impacts.

Since the particles used in these experiments are small, a large number of impacts per unit area is required to inflict a significant amount of damage. Therefore, target geometry must be chosen so as to minimize the bombardment time required, and, at the same time, the geometry must be compatible with the measurement of emissivity. The target area chosen was a 3 mm by 15mm strip on the surface of a 22 mm diameter disc. The center line was displaced 3 mm from a diameter of the disc. The strip geometry was obtained by moving the target in a plane perpendicular to the direction of the particle beam. At the beginning, only horizontal motion was used and the beam was defocused to 3 mm diameter. This was found to give non-uniform crater coverage. Later, vertical scanning was added and used in conjunction with a sharply focused beam. The horizontal motion was supplied by a motor-driven, spring-loaded cam which was machined to give constant scan velocity across the beam. Vertical motion was imparted to the target by a cam which was driven from the same shaft. In the final version, the target was moved vertically in eight discrete steps. Scanning was cyclical in both directions with the entire target area being scanned every eight minutes.

Photographs of the apparatus are shown in Figs. 6, 7, and 8. Figure 6 is an over-all view of the laboratory. The target chamber, which is at the center of the picture, is located at the end of the accelerator drift tube. The drift tube can be seen beneath the pumping line running from the target chamber to the vacuum system. The monitor oscilloscope is at the right with the Van de Graaff control console behind it.

Relay racks containing the X-Y plotter, counters, and other apparatus are in the background.

A close-up view of the target chamber is shown in Fig. 7. The vacuum pumping line is coupled to the chamber by a bellows which allows a limited degree of vertical motion for alignment purposes. The target drive motor, drive shaft, and controls are to the left of the bellows.

Figure 8 shows the target chamber with the back cover removed. The end of the particle detector can be seen immediately in front of the rectangular target holder. The target is affixed to the opposite side of the target support structure which, in turn, is fastened to the horizontal drive rod. The drive rod is spring-loaded against the nylon cam at the left. The vertical stepping cam, located beneath the target holder, is driven by the right angle gears at the left. The detector pre-amplifier is fastened to the inside top of the chamber.

B. Radiation Measurement Phase

A brief discussion of the equipment and techniques used in the measurement of optical properties is given below.

The samples are circular discs, 22 mm in diameter and 1.5 mm thick. The area of bombardment is a rectangle approximately 12 x 3 mm, the long dimension of which is parallel to, and displaced by 3 mm from a diameter. The optical instruments, which are used to measure the reflectance of the samples, are adjusted so that this off-center area is measured. The sample can be rotated 180° in the sample holder, and the unbombarded area is available for measurement. Three reflectance measurements are made:

1. The reflectance before the sample is put in the bombardment chamber.

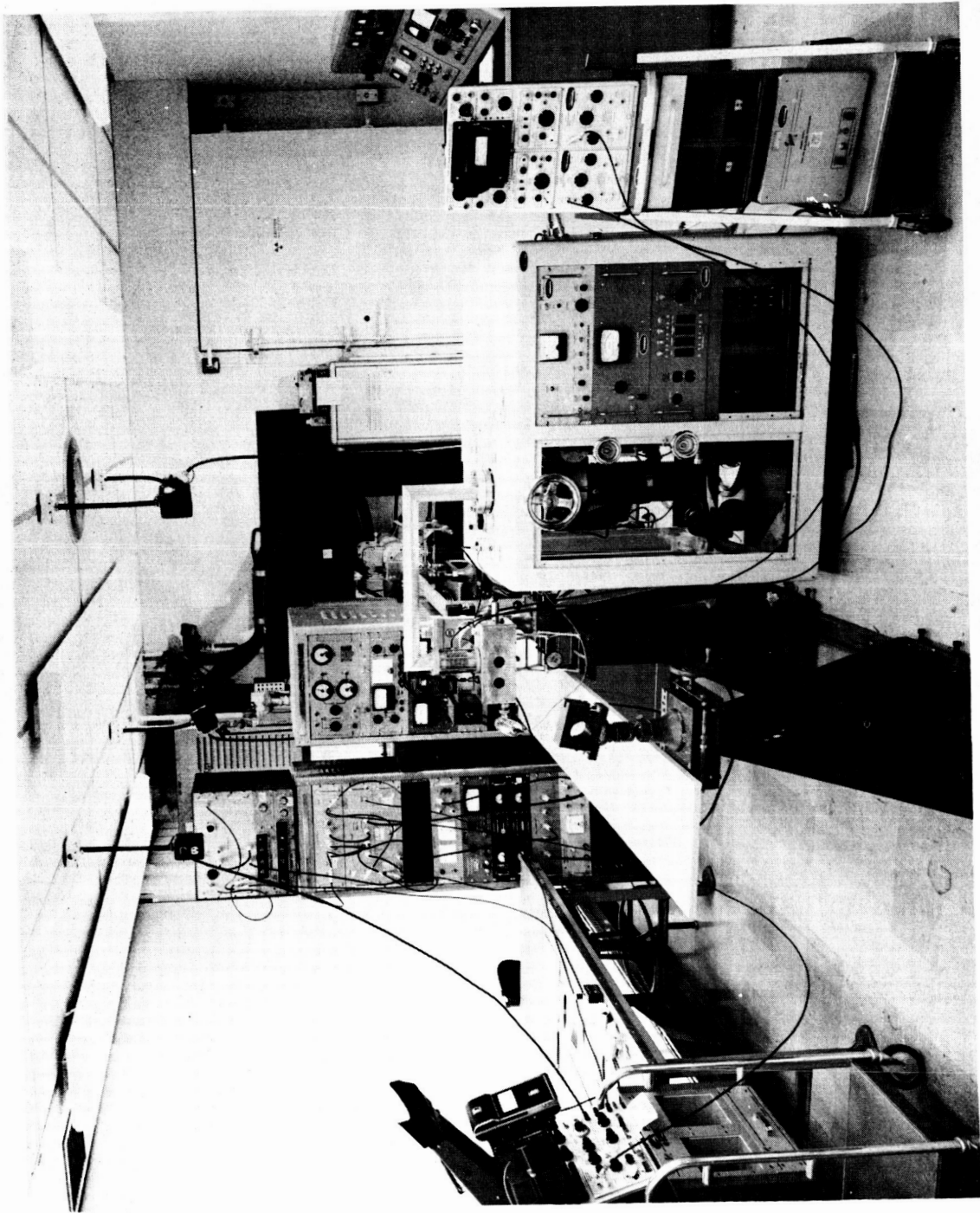


Figure 6. Over-all View of the Target Bombardment Apparatus.

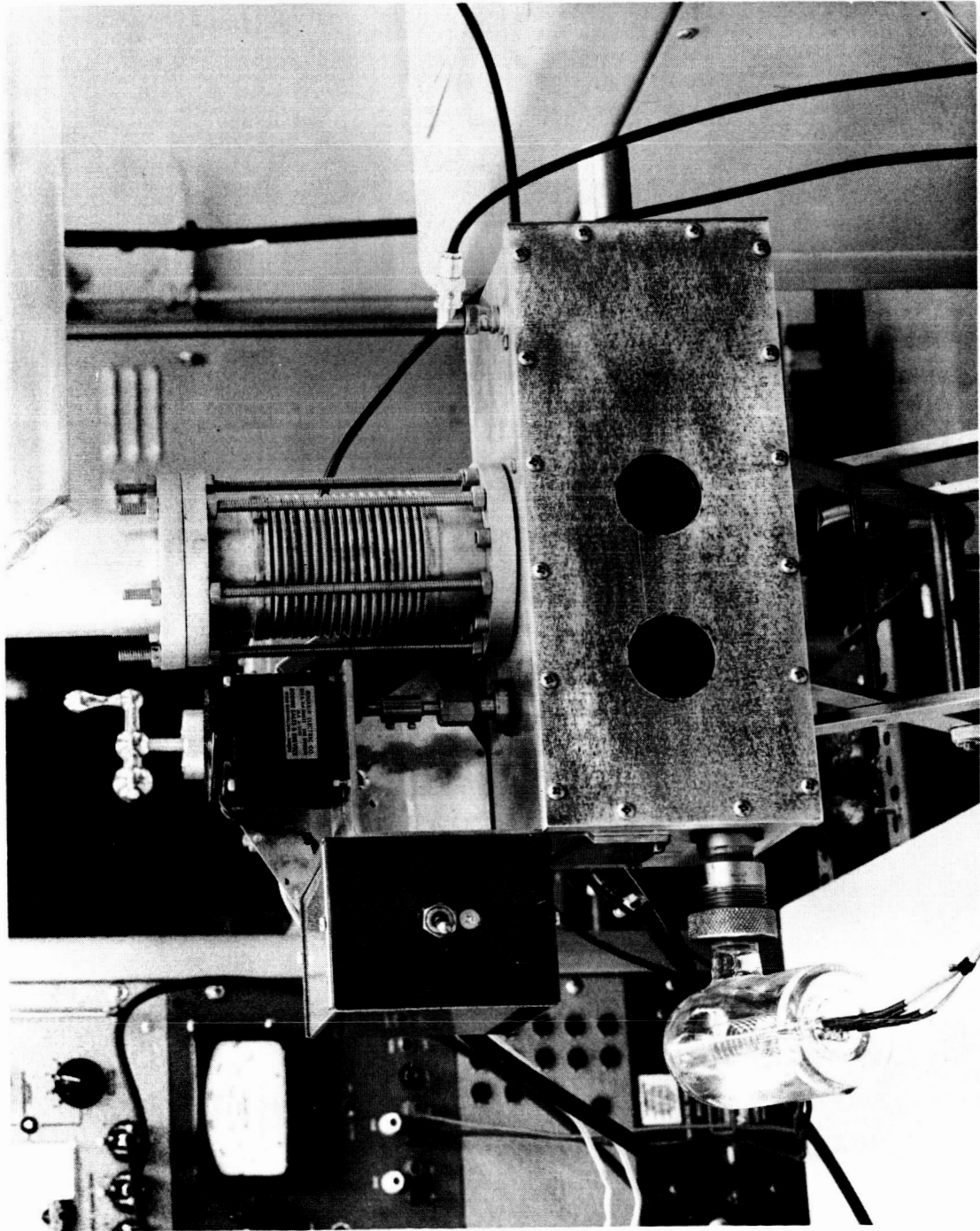


Figure 7. Exterior View of the Target Bombardment Chamber.

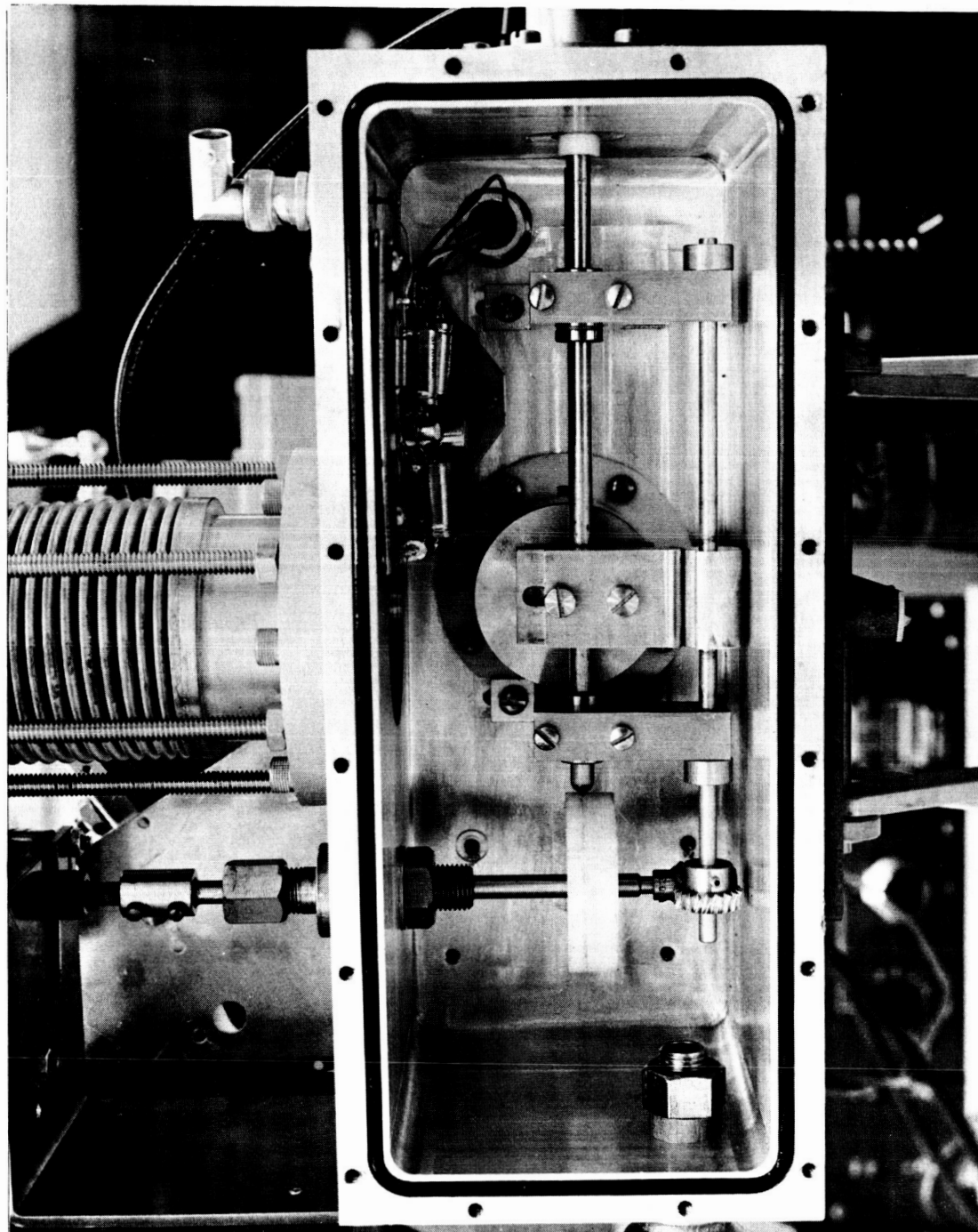


Figure 8. Interior View of the Target Bombardment Chamber.

2. The reflectance of the bombarded sample area.
3. The reflectance of an area of the sample adjacent to the damaged area, i.e., exposed to the environment.

The comparison of 1 and 3 allows the determination of effects of handling on the sample.

Two absolute reflectance measuring instruments are available for the above measurements. The Gier-Dunkle Integrating Sphere Absolute Reflectometer (Fig. 9) measures reflectance from 0.3 to 3 microns. The integrating sphere in the Gier-Dunkle Reflectometer is based upon the design of Edwards, et al.³ The Gier-Dunkle instrument has built-in features which allow measurement of the uniformity of the sphere coating, and hence, a verification of the accuracy of the measurements. The model of the reflectometer which was used for the measurement of micrometeoroid bombarded samples differed slightly from that shown in Fig. 5 of Reference 3. The source and detector assemblies are interchanged and the monochromator is internally chopped. The optical system allows the sample or the wall to be irradiated as desired without the necessity of rotating or translating the sphere. No actual modification was made in the optical system in order to measure the micrometeoroid bombarded samples. The slit was focused exactly at the bombarded area of the sample and was kept constant at 1.0 millimeter. The long wavelength (2 to 25 microns) spectral region reflectance is measured with a Gier-Dunkle Heated Cavity Absolute Reflectometer⁴ (Fig. 10). Figure 2 of Reference 4 shows the schematic diagram of the reflectometer. At the point labeled SLIT, a narrow slit was introduced and oriented so as to restrict the radiation incident on the monochromator entrance slit to that originating from the bombarded area of the sample. This does not alter appreciably the solid angle within which the sample is viewed by the monochromator.

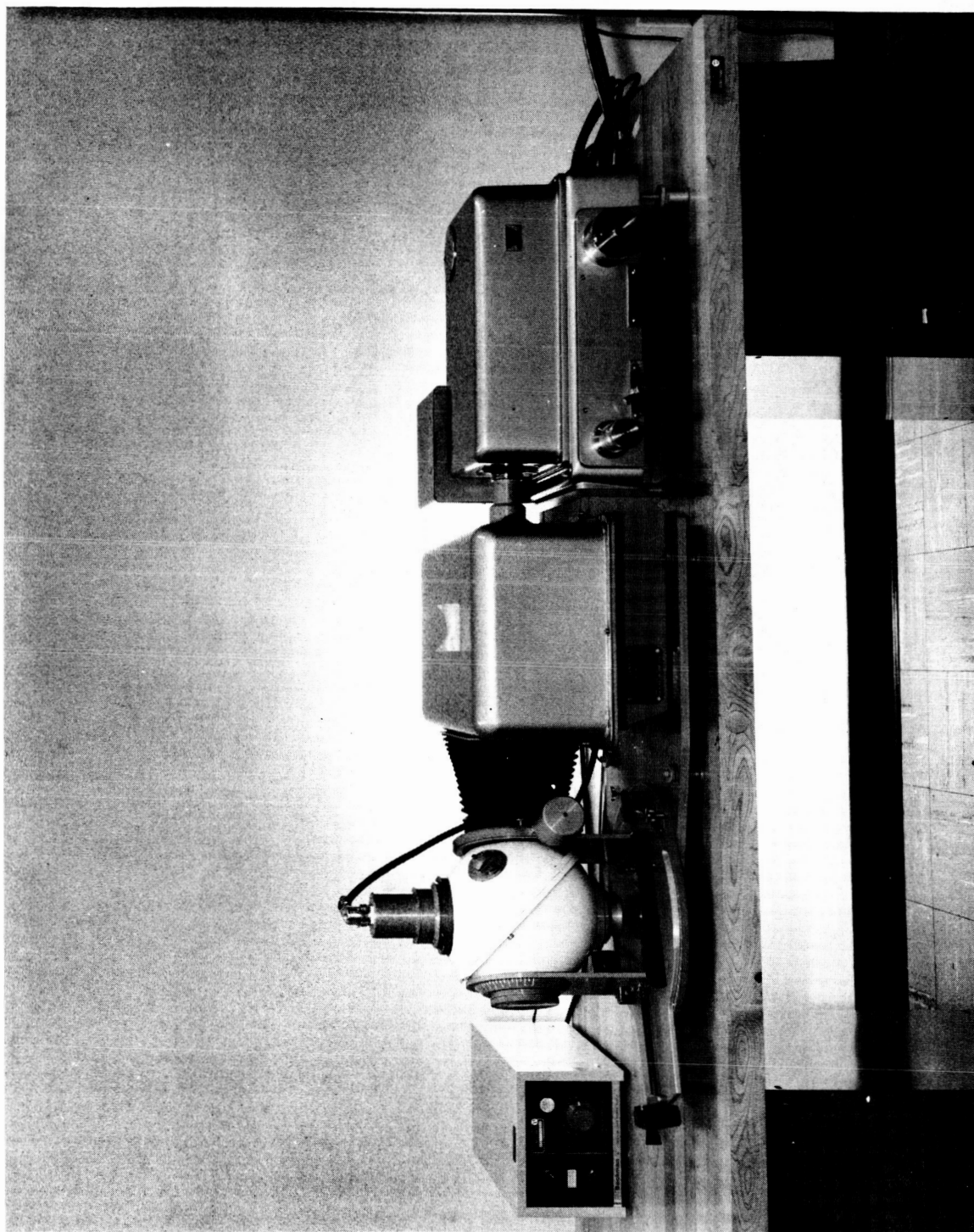


Figure 9. The Gier-Dunkle Integrating Sphere Absolute Reflectometer.

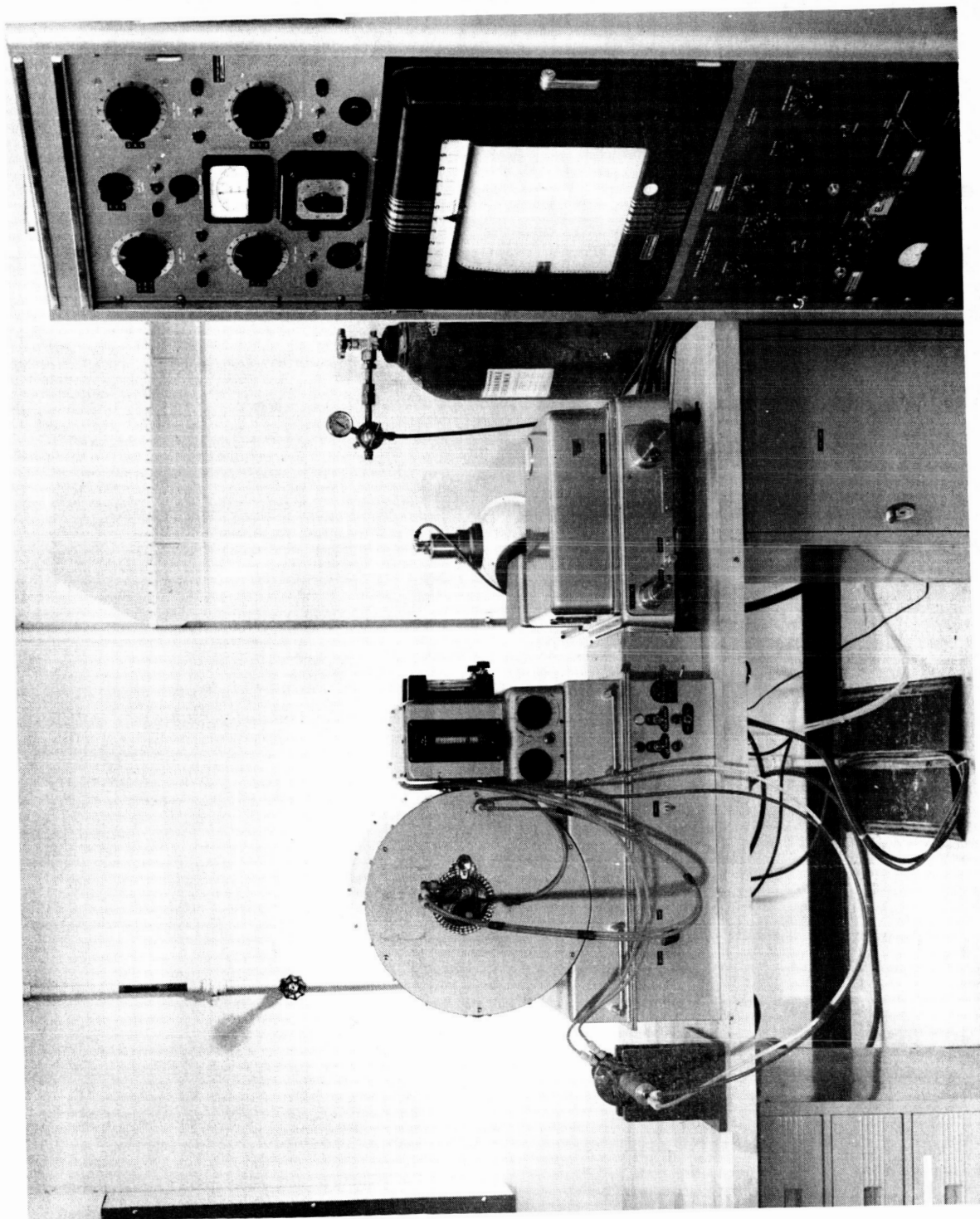


Figure 10. The Gier-Dunkle Heated Cavity Absolute Reflectometer.

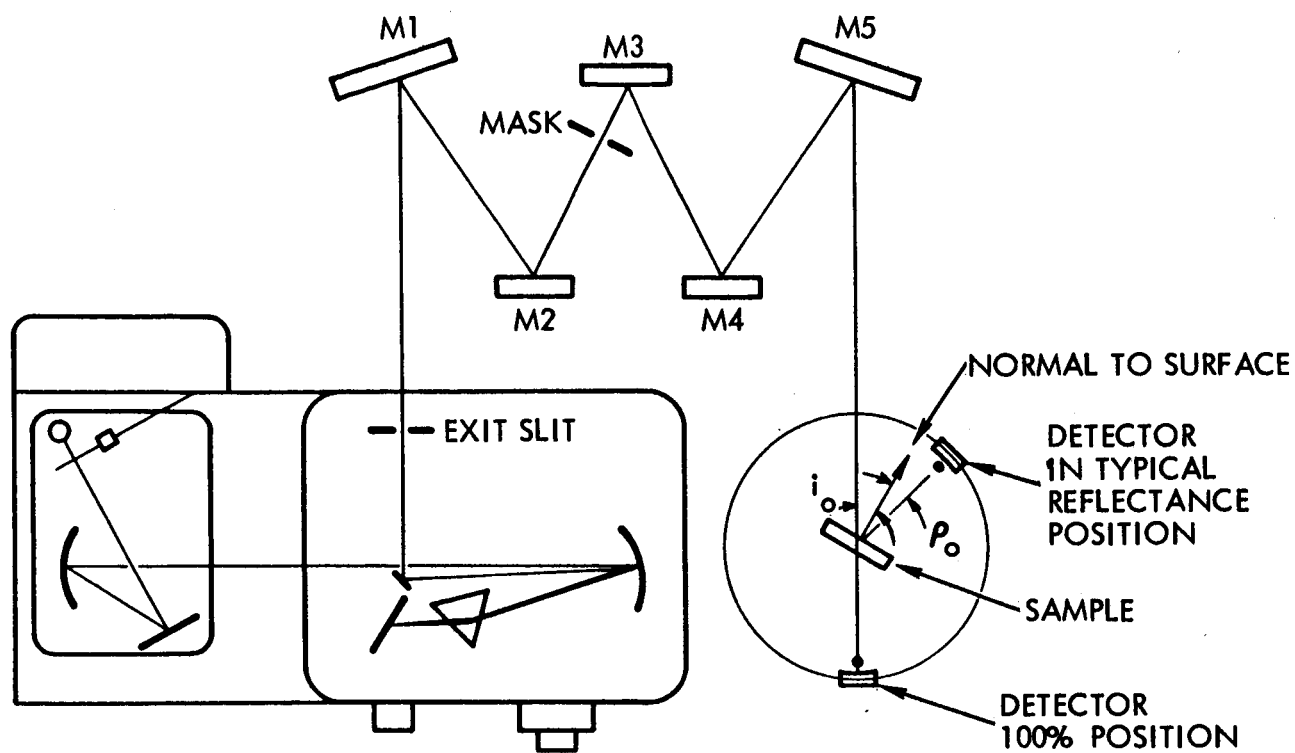
Both of these instruments measure directional spectral reflectance.⁵ By suitable integration, solar absorptance and normal emittance (at ambient temperature) can be computed. By making certain assumptions,⁶ a correction can be calculated which provides the hemispherical emittance as a function of the normal emittance. Experimental data showing the relation of normal-to-hemispherical emittance are quite limited. As the data in Ref. 6 show, this theoretical correction does not apply very closely to some materials, particularly roughened metals. One method which will yield a more valid correction for the normal-to-hemispherical emittance is the measurement of the reflectance distribution function.⁷

The specular reflectance measurements were made on the STL Goniometric Bi-directional Reflectometer (Fig. 11). In this device, the sample can be irradiated at any polar angle between zero and approximately 80 degrees; the azimuthal angle is unrestricted between 0 and 360 degrees. The detector of the reflected energy may be positioned at any angle measured from the sample normal from zero to approximately 80 degrees (excluding interference with the incident energy). In addition, the normal to the sample may be tilted out of the plane containing the irradiation and detector beams. These four degrees of freedom permit the angle of incidence and reflectance to be varied with only limited constraints upon the azimuthal and polar angles. In practice, the sample image size (incident energy) determines these limits. The specular reflectance is measured by setting the angle of the detector equal to the angle of irradiation but on the opposite side of the normal to the sample.

The Goniometric Bi-directional Reflectometer is shown schematically in Fig. 12. The monochromator and source assembly is a Perkin-Elmer Model 12C spectrometer. The dispersed energy from the spectrometer is collected from the exit slit by

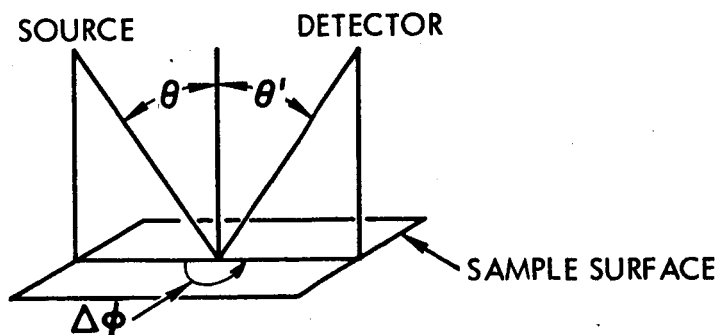


Figure 11. The Goniometric Bi-Directional Reflectometer.



PERKIN-ELMER MODEL 12C

M1, M5 SPHERICAL MIRRORS 300 mm.f.l.
M2, M3, M4 FLAT MIRRORS



WHEN $\Delta\phi = 180^\circ$, $i_o = \theta$ AND $\rho_o = \theta'$

Figure 12. Schematic Diagram of the Goniometric Bi-directional Reflectometer.

mirror M1. The first image of the exit slit occurs near M3. A mask is introduced into the beam at this point to control the size of the final image on the sample. The first image is re-imaged by spherical mirror M5 onto the sample. In order to obtain the hundred percent reference, the sample is removed from the optical path and the radiation is incident on the detector-mirror assembly. The sample is interposed in the optical path as shown and the detector assembly rotated about the sample in order to intercept the specular reflection from the sample. The sample may be translated in the holder so that either the bombarded or unbombarded area is irradiated. The irradiating beam subtended a solid angle of 0.01 steradian at the sample. The detector mirror subtends a solid angle of 0.1 steradian at the sample.

In operation, the incident reference energy is obtained by setting the incident beam and detector beam 180 degrees apart and removing the sample from the optical path. The detector is then positioned at the desired angle of reflection. For the measurements reported herein, this angle was 15 degrees from the normal and the sample was placed at zero tilt to the incident energy. The reflectance of the bombarded and unbombarded areas was measured in this manner. For a perfectly specular surface, the value of reflectance by this instrument should be the same as the directional reflectance measured with either an integrating sphere or heated cavity reflectometer. The scattering (diffusing) effects of the micrometeorite roughening would be indicated by a decrease in the value of the specular reflectance. For the tests reported, the samples were measured at each micron increment from 2 to 15 microns.

All of the instruments described above are designed for measurements with sample areas of approximately 22 mm in diameter. In order to measure the reflectances of the micrometeoroid bombarded samples, certain modifications have had to

be made to accommodate the small area of damage (3 x 12 mm). The modification required for the Gier-Dunkle Heated Cavity has been the introduction of a limiting aperture at the first image of the monochromator entrance slit. This decreases the energy available for the measurements, and hence, the usable wavelength region is reduced to 20 microns. The operation of the Gier-Dunkle Integrating Sphere Absolute Reflectometer is modified by maintaining a slit opening in the monochromator of one millimeter. This does not affect the measurements below 2 microns.

C. Target Damage Assessment

As mentioned above, the damage inflicted upon the target surface was specified in terms of the fraction of total target area covered by craters. The surfaces of selected samples were photographed using a high power metallographic microscope. The magnification was either 500X or 1000X, depending upon the sample material. The surface was photographed at ten or twenty randomly selected areas to minimize the influence of local non-uniform coverage. Typical photographs are shown in Figs. 13 through 15. Figure 13 shows two different gold targets after bombardment by 100,000 and 400,000 particles, respectively. Figure 14 shows photographs of two stainless steel targets after bombardment by 300,000 and 600,000 particles. Similar photos for vacuum deposited aluminum are shown in Fig. 15.

Crater diameters (including the lip) were measured from the photographs using the Telereader and plotted in histogram form, as illustrated in Figs. 16 and 17. The crater area per interval was calculated using the mean diameter for each interval. The area covered by craters was obtained by summing over all of the intervals. Since the target area represented by the photographs is known, the fractional area covered by craters is determined.

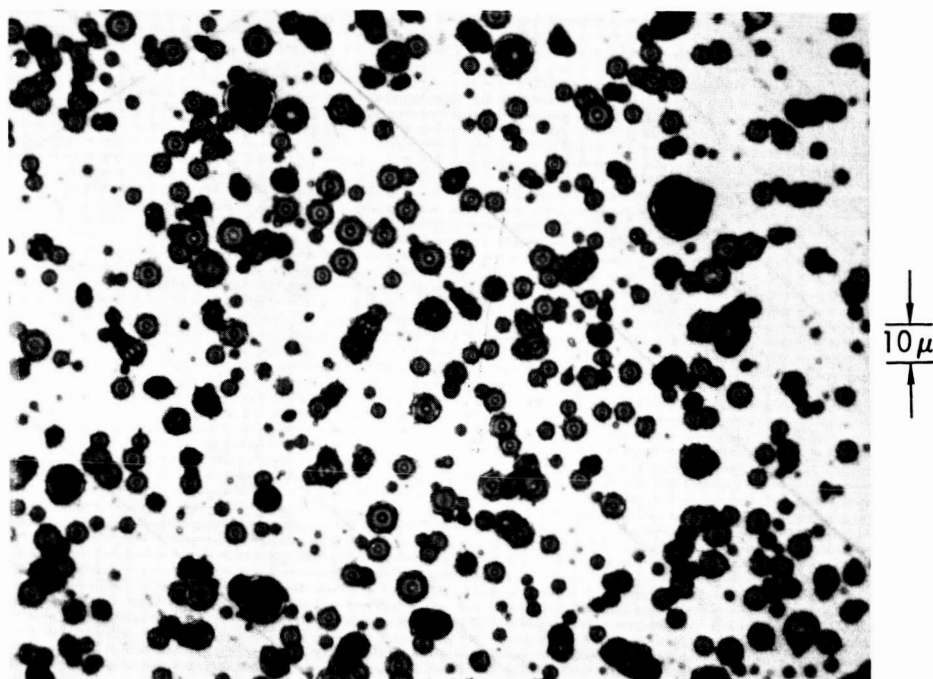
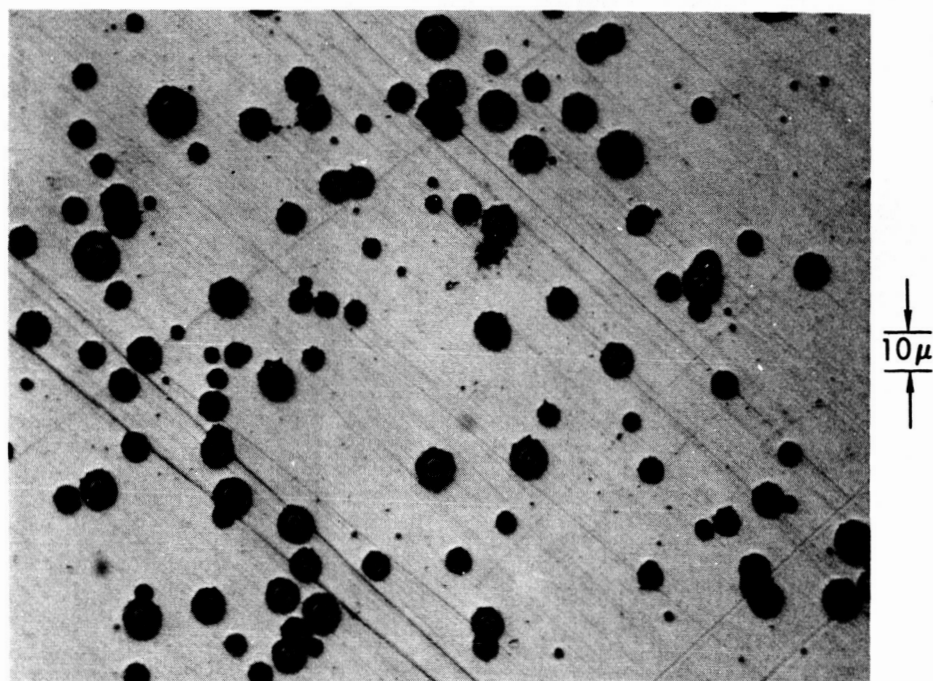


Figure 13. Photographs of Gold Targets. The upper and lower photographs were taken after bombardment by 100,000 and 400,000 impacts, respectively. Magnification is 500X in both cases.

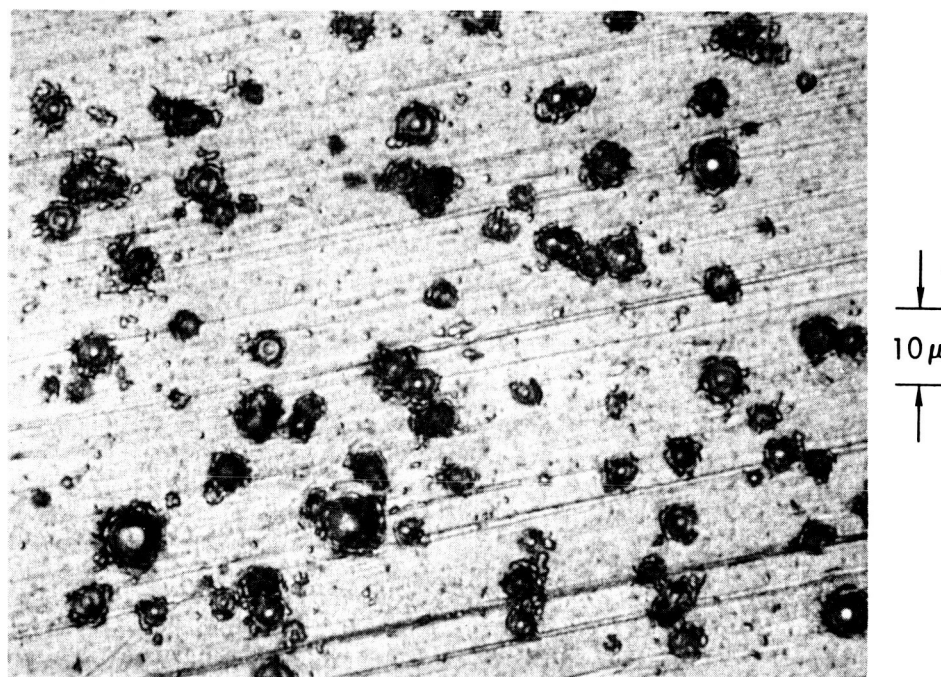
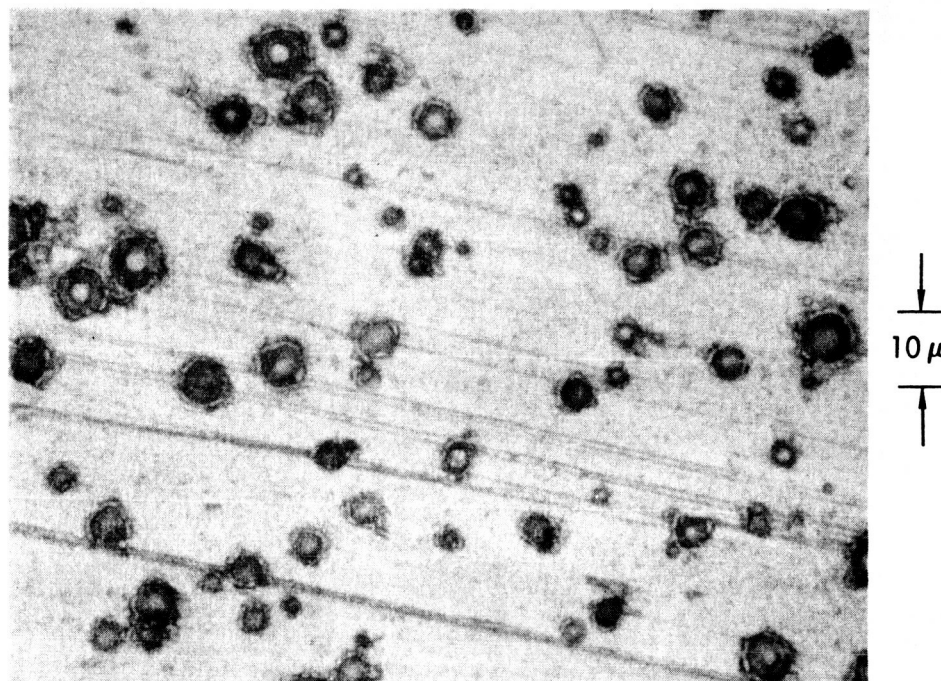


Figure 14. Photographs of Two Stainless Steel Targets After Bombardment by 300,000 Particles (upper) and 600,000 Particles (lower). Magnification is 1000X.

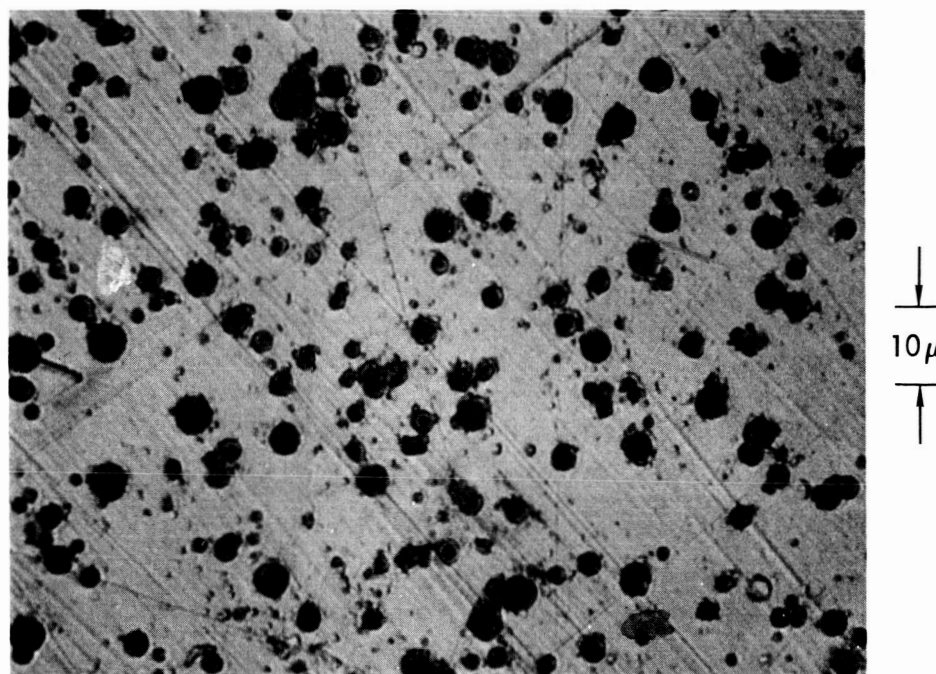
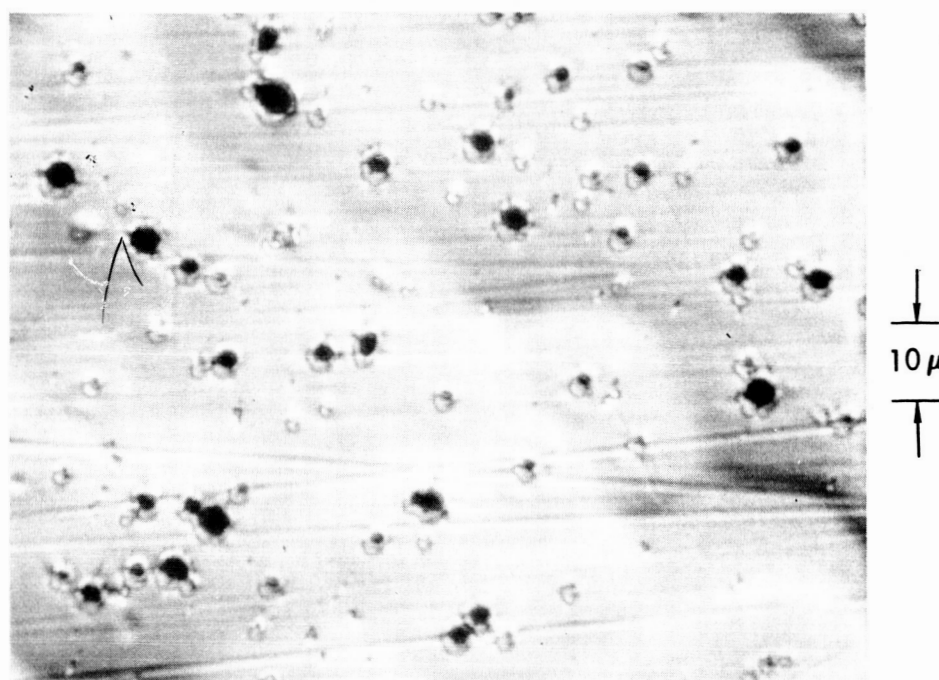


Figure 15. Photographs of Vacuum Deposited Aluminum after Particle Bombardment. The upper photo followed bombardment by 300,000 particles while the lower was taken after 600,000 impacts. Magnification is 1000X.

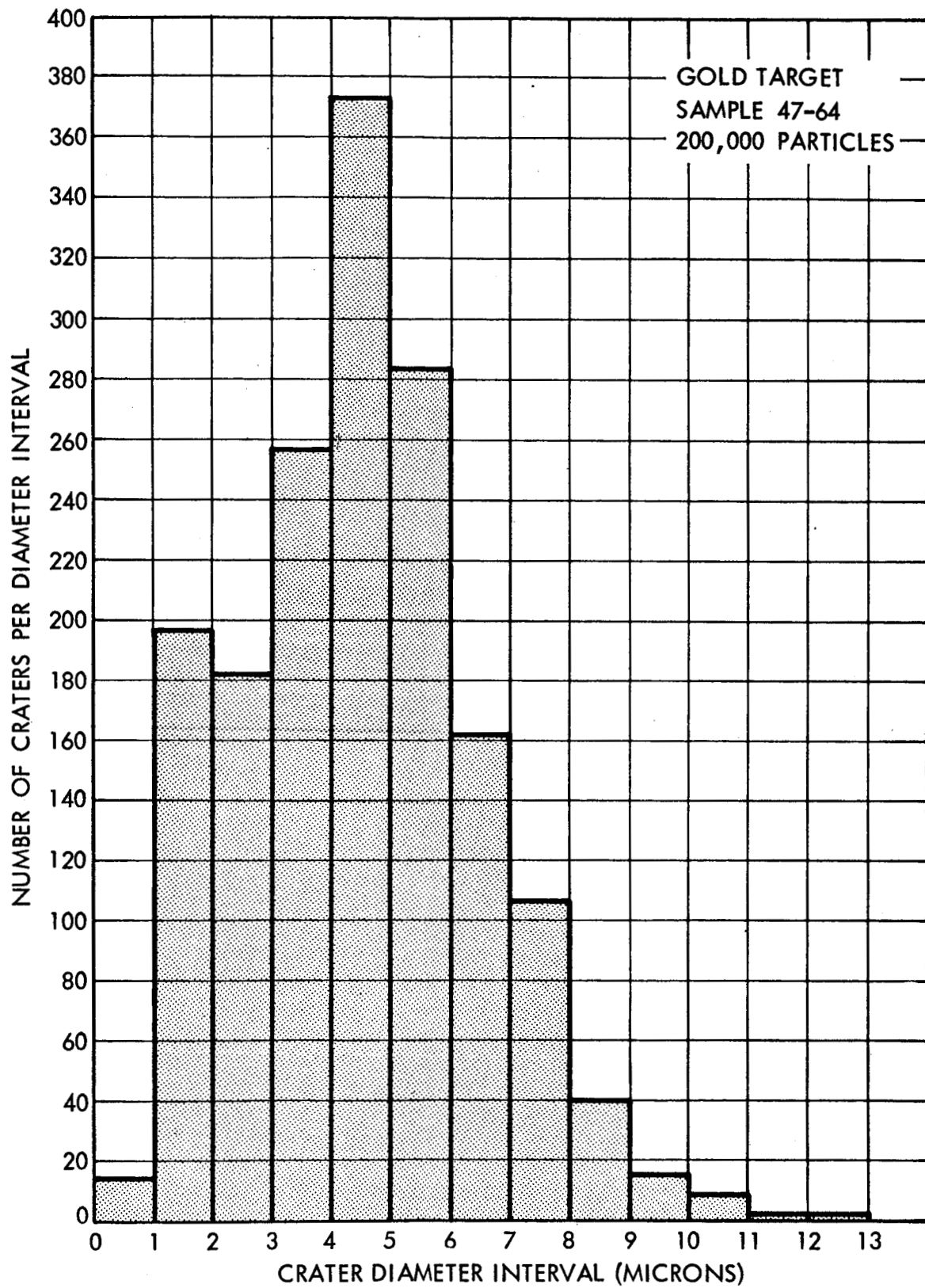


Figure 16. Histogram of Crater Diameters for a Gold Target.
(Sample 47-64)

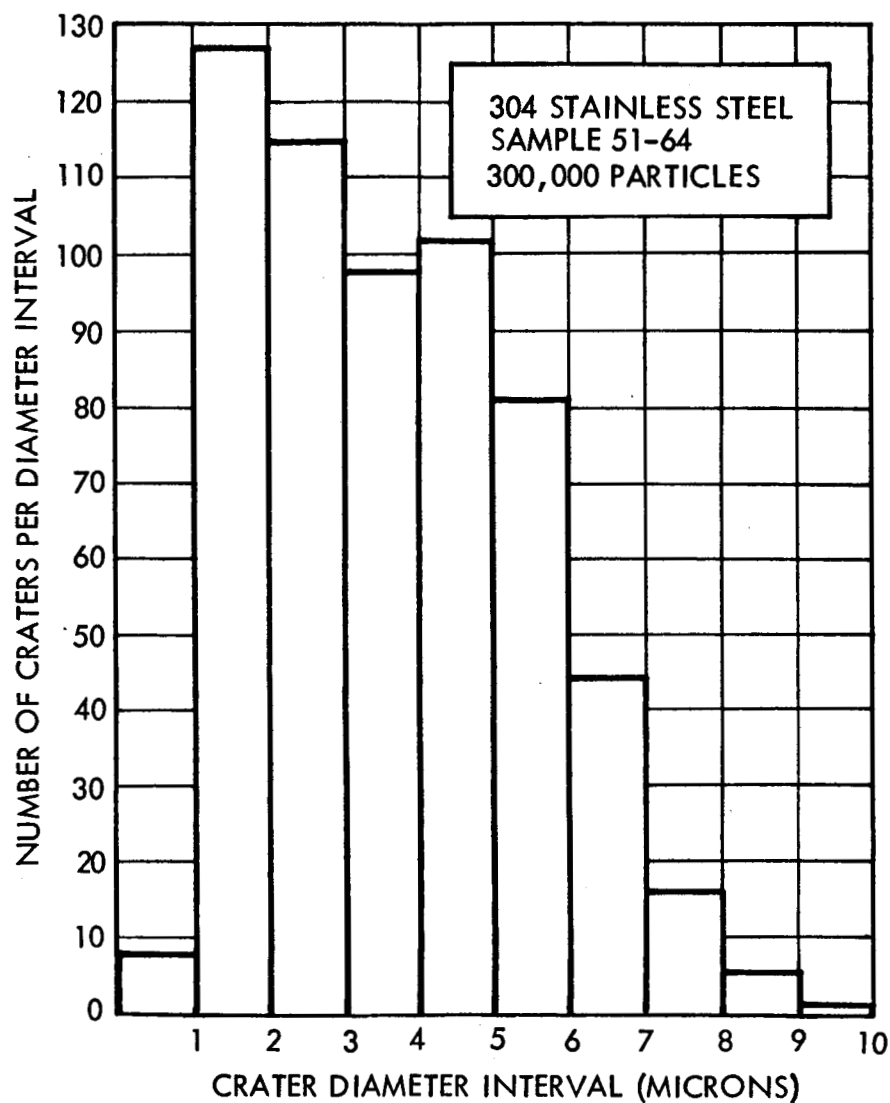


Figure 17. Histogram of Crater Diameters for a Stainless Steel Target (Sample 51-64).

Implicit in the preceding paragraph is the fact that target damage is determined by statistical techniques. Efforts were made to obtain samples on a sound basis and it is felt that the estimates are adequate. This procedure was not applied to all targets. Several gold and stainless steel targets were analyzed and coverage for other targets of the same materials were estimated from the measured values. Less accurate measurements of crater diameters are obtained for the smaller craters since their diameters are near the resolution limit of the equipment. This is illustrated in Fig. 17 which is a crater size histogram for a stainless steel target. There are a large number of craters in the 0 to 2 micron range. However, the area per crater in this range is quite small and errors in measurement do not significantly effect the calculated coverage.

The vacuum deposited aluminum targets were not evaluated in the same manner because of the peculiar nature of the craters. For some craters, penetration into the resin substate is apparent while for others this is not the case (see Fig. 15). Since penetration into the resin reveals material of a markedly different emissivity, it was felt that a simple area specification was not meaningful. Accordingly, the damage for the vacuum deposited aluminum targets is specified only in terms of the number of particle impacts. Furthermore, there is reason to believe that the craters in resin are not hemispherical. Instead, they are likely to be relatively deep and narrow as has been observed for plastic targets by numerous experimenters.

III. EXPERIMENTAL RESULTS

A. Emissivity Measurements

The changes in emittance for a temperature of 25°C are tabulated in Table I for the various samples; the corresponding spectral reflectance curves are given in Figs. 18 through 23. The primary materials studied were gold plated aluminum, type 304 stainless steel and vacuum deposited aluminum on a resin coating over aluminum. The difference between the damage to these three surfaces is very noticeable. The percentage increase in emittance ($\Delta\epsilon/\epsilon$) is greatest with the gold plated samples; the stainless steel had the least change. For 100,000 impacts, the vacuum deposited aluminum on a resin coating exhibited a greater resistance to micrometeoroid roughening than either the gold or stainless steel. The data for this material after 100,000 impacts is not included since there are virtually no changes exceeding the experimental error. However, as the exposure was increased, the change in emittance ($\Delta\epsilon$) for this material became more nearly equal to that of the gold and the stainless steel. A cause for this resistance at the lower number of impacts may be hypothesized in terms of the resilience of the resin. After continued bombardment, the lower emittance resin probably became exposed sufficiently to change the emittance. This was observable to a certain degree under the microscope.

The stainless steel material exhibited less emittance change than the gold for a larger number of impacts. This is attributable to the differences in the physical properties influencing hypervelocity damage in the two materials. The areal damage per particle is a measure of the average crater size per particle. Hence, the smaller damage exhibited by the stainless steel is consistent with the smaller emittance change.

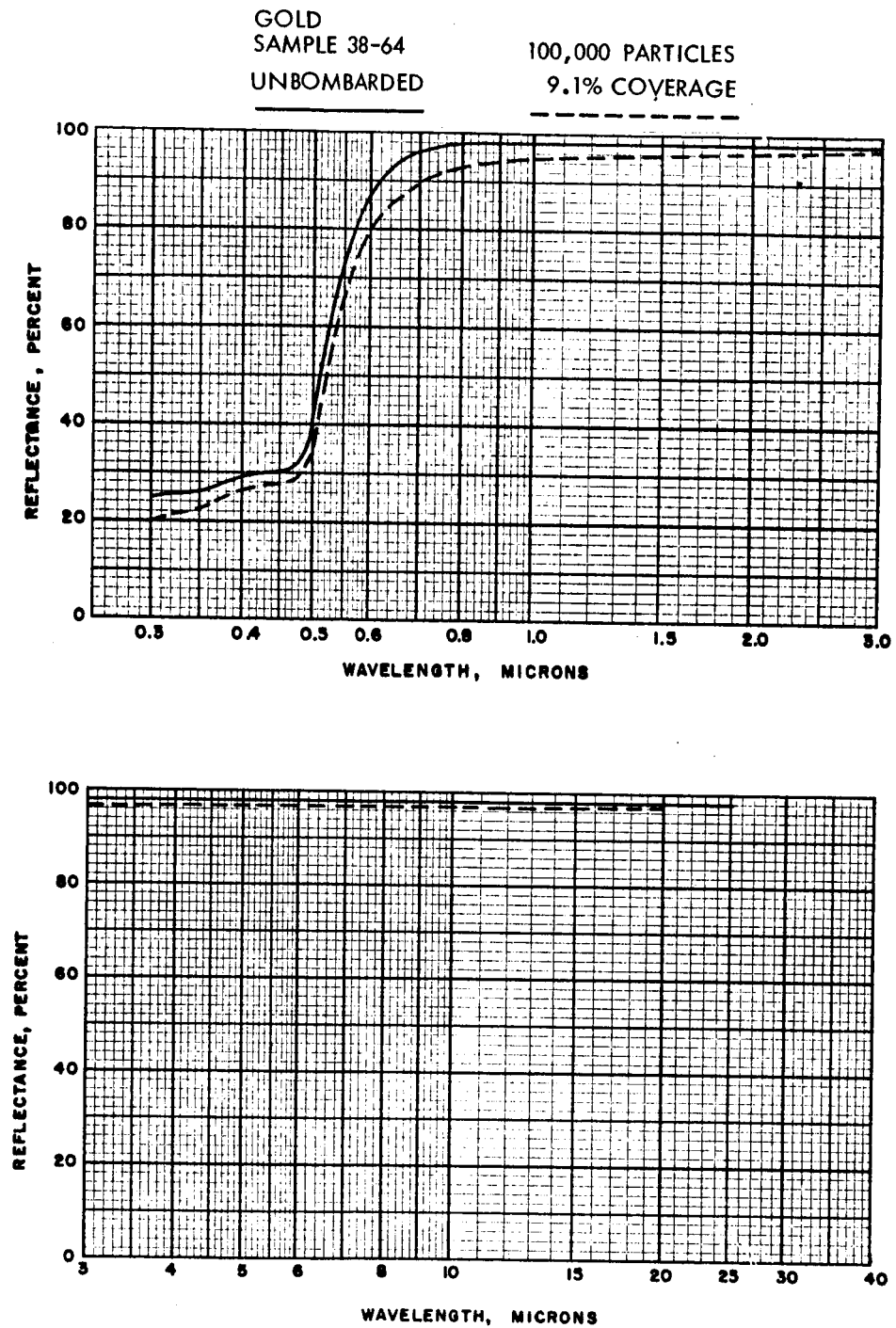


Figure 18. Spectral Reflectance of a Gold Sample Before and After Particle Bombardment.

GOLD		
SAMPLE 47-64	200,000	400,000 PARTICLES
UNBOMBARDED	15.1 %	30 % COVERAGE
	-----

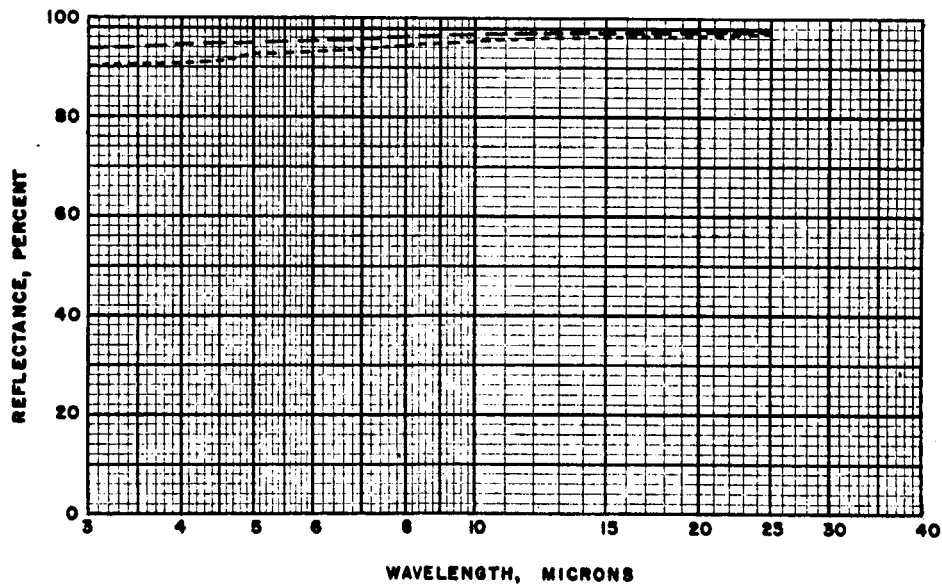
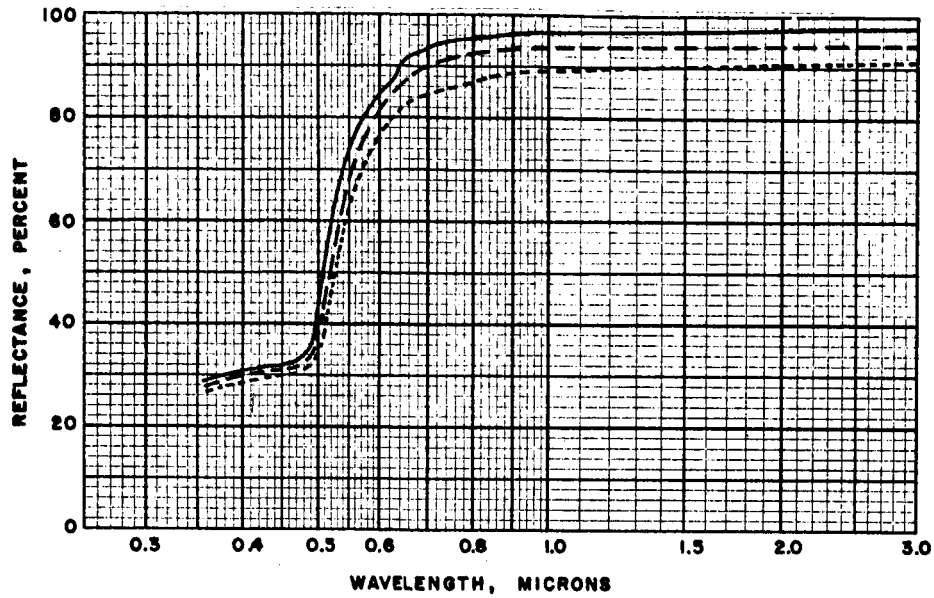


Figure 19. Spectral Reflectance of a Gold Sample Before and After Particle Bombardment. The bombardment was done in two steps as shown.

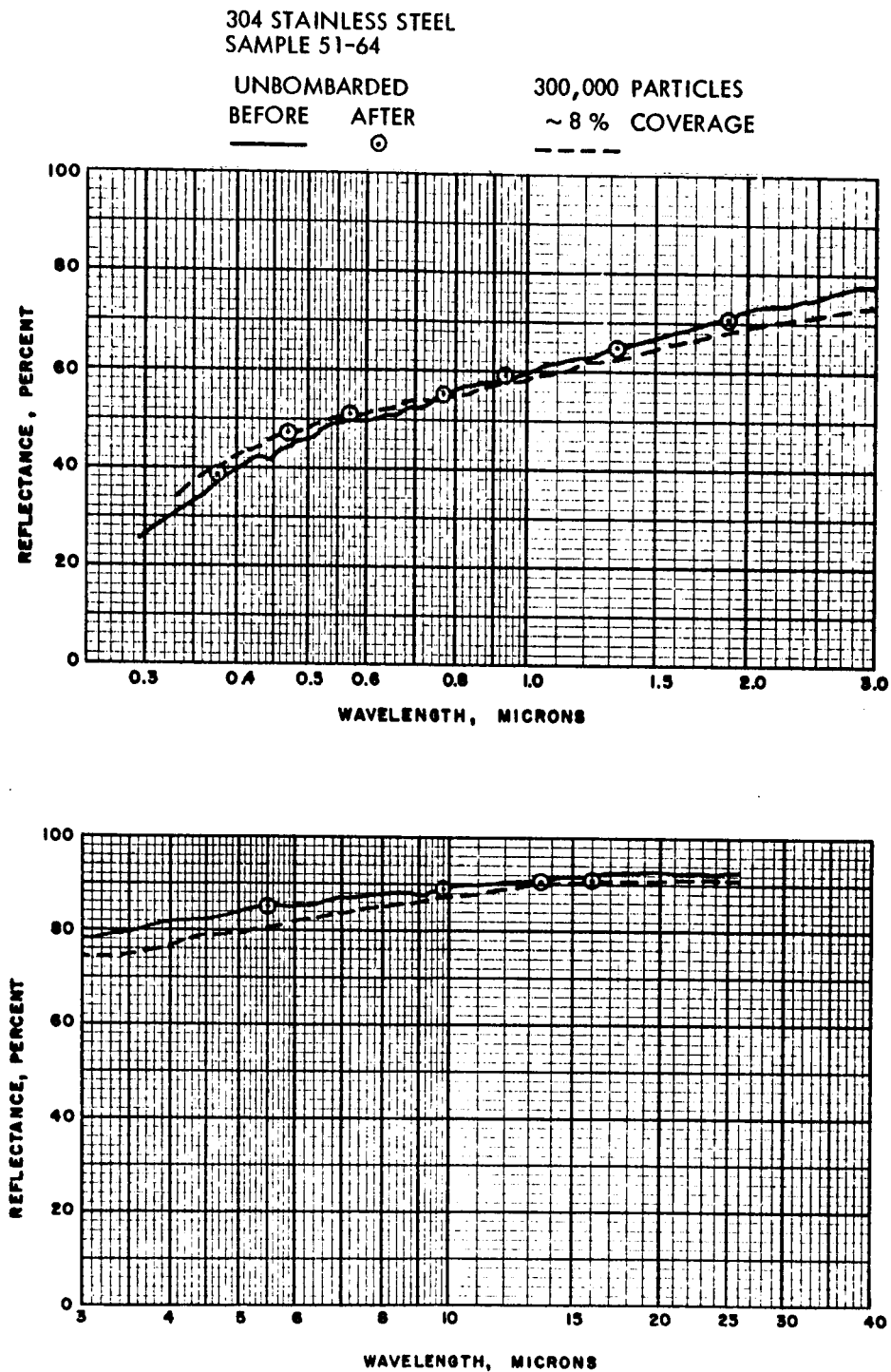


Figure 20. Spectral Reflectance of a 304 Stainless Steel Sample Before and After Particle Bombardment.

304 STAINLESS STEEL
SAMPLE 97-64
UNBOMBARDED

600,000 PARTICLES
~16 % COVERAGE

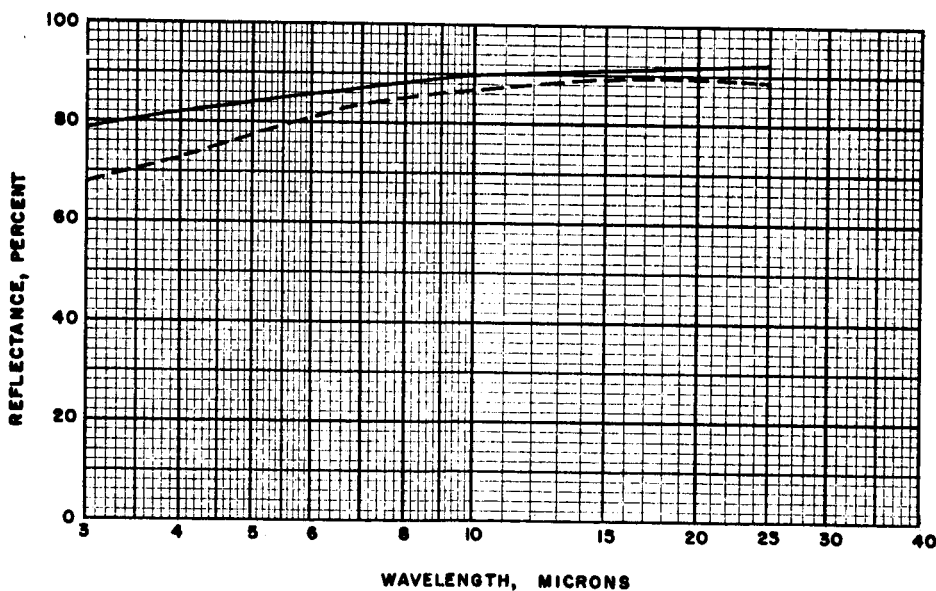
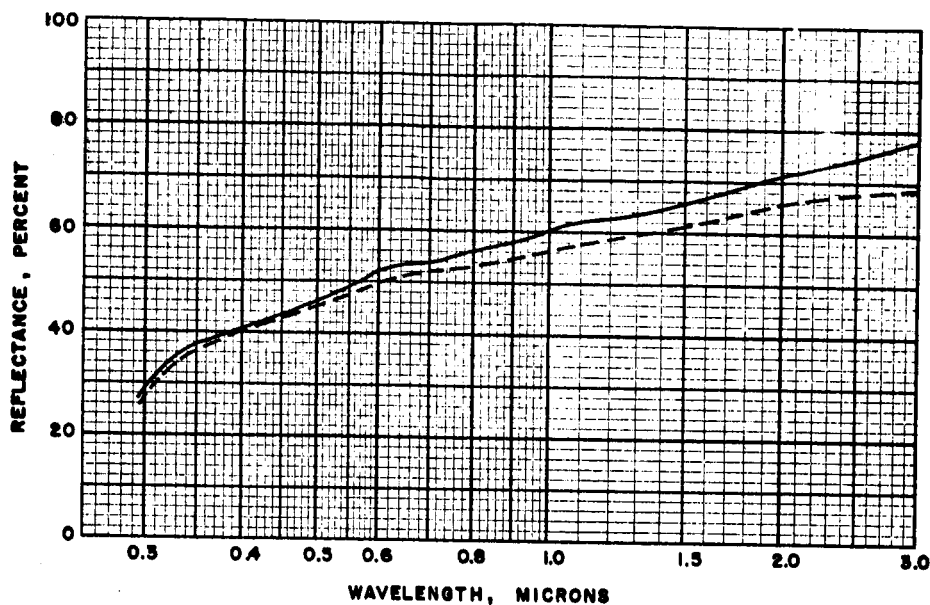


Figure 21. Spectral Reflectance of a 304 Stainless Steel Sample Before and After Particle Bombardment.

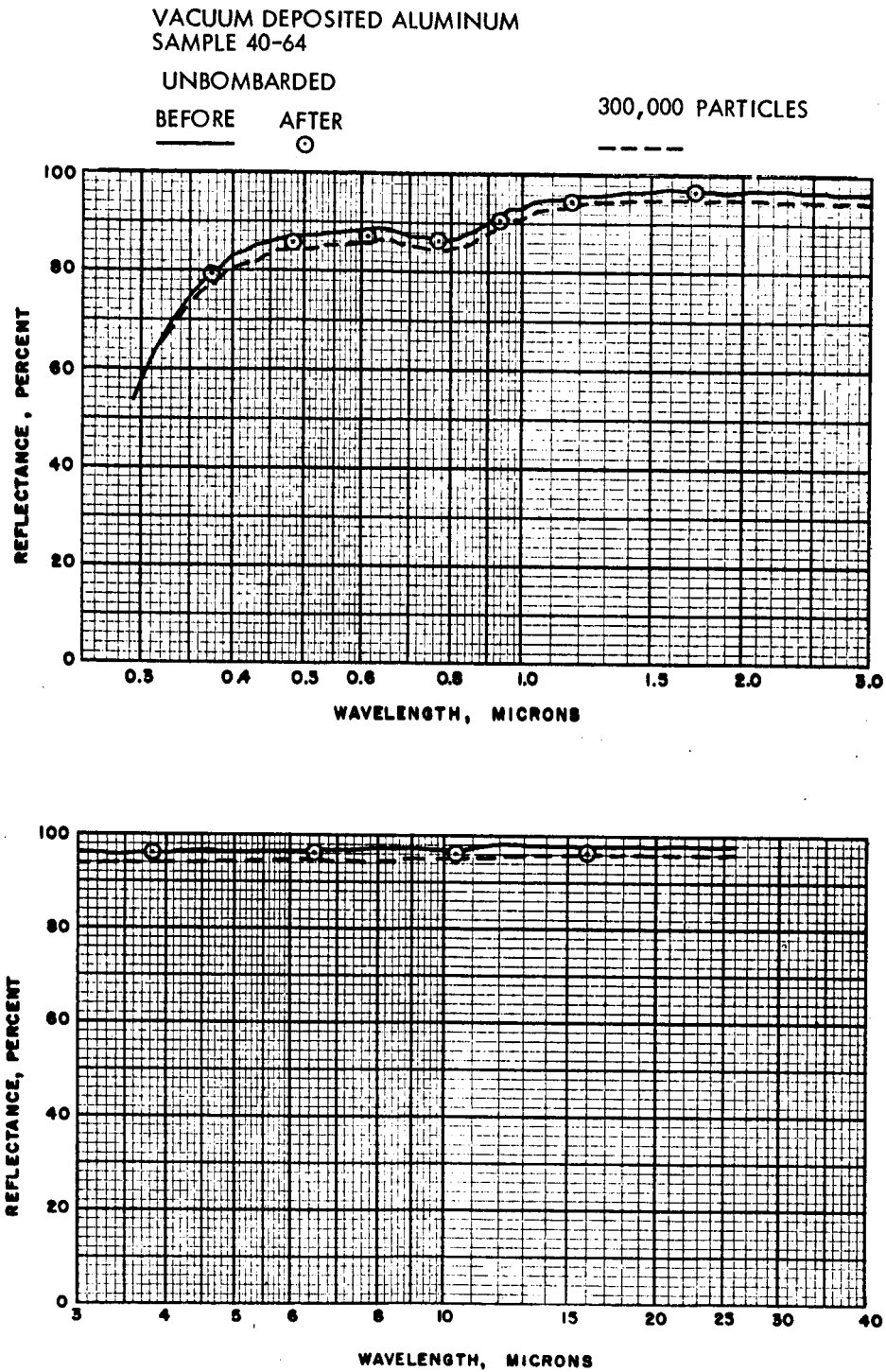


Figure 22. Spectral Reflectance of a Vacuum Deposited Aluminum Sample Before and After Particle Bombardment.

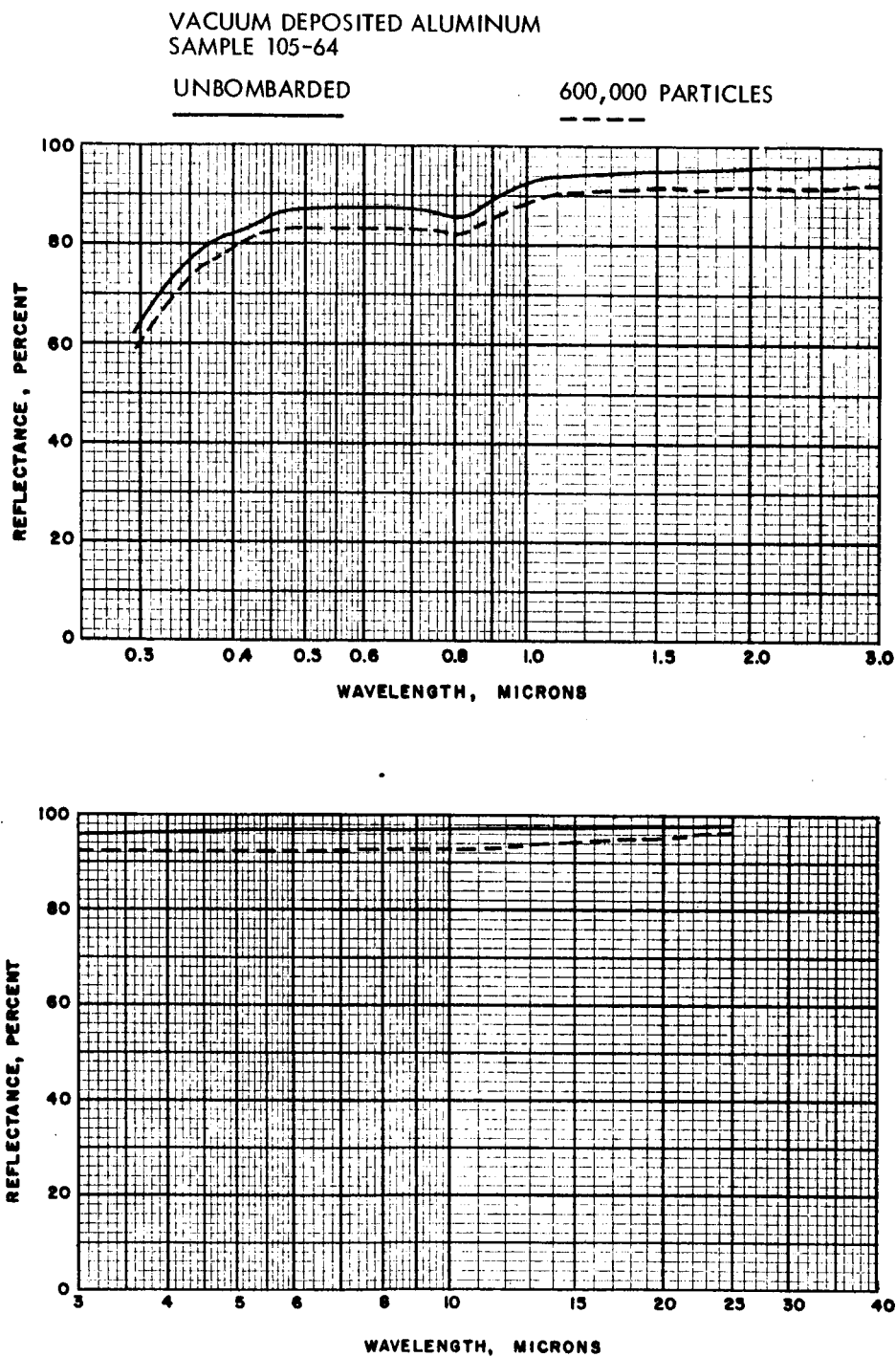


Figure 23. Spectral Reflectance of a Vacuum Deposited Aluminum Sample Before and After Particle Bombardment.

Cadmium plated aluminum and tin plated aluminum were originally selected as sample materials. These materials were chosen to obtain a wider range of the physical properties pertinent to hypervelocity damage. Unfortunately, optical measurements made with these surfaces were not found to be consistent. This is believed to be a result of the readiness with which these surfaces formed oxides that were important optically, i.e., unlike aluminum. Part of the inconsistency was believed to be the result of exposing "fresh" material during the bombardment process. This exposed material developed an oxide coating differing in age from the reference area of the sample.

The use of a reference area on the sample proved to be quite important. Because of handling during the bombardment and optical measurement, the thermal radiation properties of the sample may become altered. Since the changes that are being measured are often of the order of 1 to 2 percent, environmental effects can mask the results of bombardment. The circled points in Fig. 22 illustrate such small effects.

The presentation of the data in terms of spectral reflectance should not obscure the magnitudes of the changes in emittance or absorptance. The integrated properties for the various curves are summarized in Table I. Metal surfaces are primarily used in space vehicle thermal control to minimize heat lost by emission. If, as in several cases given in Table I, the emittance increases by a factor of 2, the intended purpose may be voided. The increase in solar absorptance noted for all samples may partially offset the emittance change in certain thermal control applications. Further generalizations relative to the effect of micrometeoroid bombardment (real or simulated) are not possible. Only for specific thermal control applications can valid qualitative or quantitative conclusions be reached relative to the effect of the bombardment.

TABLE I
EFFECT OF SIMULATED MICROMETEORITE BOMBARDMENT
UPON INTEGRATED DIRECTIONAL REFLECTANCE

TOTAL DIRECTIONAL EMITTANCE ($\theta = 15^\circ$) OF THE TEST SAMPLES									
DESCRIPTION				EMITTANCE			SOLAR ABSORPTANCE		
Materials	Impacts	% Coverage		Initial ϵ	After ϵ	Increase $\Delta \epsilon$	Initial α	After α	Increase $\Delta \alpha$
38-64	Gold	100,000	9.1	.02 ₀	.02 ₁	.00 ₁	.23 ₇	.27 ₃	.03 ₆
47-64	Gold	200,000	15.1	.02 ₂	.02 ₈	.00 ₆	.23 ₂	.27 ₁	.03 ₉
47-64	Gold	400,000	~30	.02 ₀	.04 ₄	.02 ₄	.24 ₀	.29 ₃	.05 ₃
51-64	304 Stainless Steel	300,000	~8	.09 ₆	.11 ₄	.01 ₈	.45 ₄	.46 ₃	.00 ₉
97-64	304 Stainless Steel	600,000	~16	.10 ₃	.12 ₈	.02 ₅	.45 ₄	.48 ₃	.02 ₉
40-64	Vacuum Deposited Aluminum	300,000	-	.02 ₃	.04 ₀	.01 ₇	.11 ₀	.13 ₀	.02 ₀
105-64	Vacuum Deposited Aluminum	600,000	-	.03 ₀	.06 ₀	.03 ₀	.12 ₀	.15 ₈	.03 ₈

NOTE: The third significant figure is given as shown because the accuracy of the measurement does not justify giving the absolute value to more than plus or minus .01. The values of the measurements relative to each other should, however, be more accurate and the small changes involved would be distorted if the values were reduced to two significant figures.

B. Specular Reflectance Measurements

The simulated micrometeorite bombardment results in a roughening of the sample surface. In addition to changing the value of the directional spectral reflectance (or emittance) of the surface, this roughening will modify the geometrical distribution of the reflected (or emitted) energy. The materials studied were, for practical purposes, specular reflectors and a measure of the geometrical change is the change in the specular reflectance. The measured effects upon specularity are summarized in Table II for the most heavily bombarded samples.

The most obvious effect of the bombardment is the large decrease in the specularity of the surfaces at wavelengths less than 8 microns. For a temperature of 25°C, these changes will have no effect upon the geometrical distribution of the emitted energy; and the effect would be negligible up to temperatures of 200-300°C. The effect upon solar absorptance will be much greater, however. Unfortunately, the necessary data were not obtained for these changes at wavelengths less than 2 microns, but it is safe to assume that the indicated trend with wavelengths will continue. Thus, the solar absorptance can be expected to become less specular. Note, however, the value of the directional solar absorptance is not altered to the same degree (Table I). The results given in Tables I and II indicate the short wavelength reflectance of the samples has become more "diffuse" but not significantly less reflective. In certain applications, this change will require consideration of both diffuse and specular properties in the solar region and the specular properties in the infrared. Thermal analysis of critical solar irradiated components may become quite difficult under these conditions.

TABLE II
EFFECT OF SIMULATED MICROMETEORITE BOMBARDMENT
UPON THE SPECULAR REFLECTANCE

SPECULAR REFLECTANCE OF BOMBARDED AREA DIVIDED BY SPECULAR REFLECTANCE OF UNBOMBARDED AREA ($\theta = 15^\circ$)			
Wavelength Microns	Gold 47-64 400,000 Impacts	Stainless Steel 94-64 600,000 Impacts	Vacuum Deposited Aluminum 105-64 600,000 Impacts
2.0	.71	.70	.87
2.95	.75	.76	.86
4.0	.80	.78	.87
5.0	.85	.87	.90
6.0	.83	.93	.90
7.0	.90	1.00	.93
7.8	.93	.98	.96
9.0	.98	1.00	1.00
9.8	.99	1.00	1.00
11.0	1.00	1.00	1.00
12.0	1.00	1.00	1.00
13.0	1.00	1.00	1.00
14.0	1.00		1.00
15.0		1.00	1.00
16.0	1.00		1.00
17.0		1.00	1.00
18.0	1.00		1.00
19.0		1.00	1.00
20.0	1.00		1.00
21.0		1.00	

C. Hypervelocity Cratering

Although not of primary concern in this program, it is possible to obtain some information on hypervelocity cratering from the test results. The distributions of crater sizes are known for most of the targets as well as the distributions of particle parameters. In principle, these distributions could be matched by the correct choice of the values of variables in a suitable hypervelocity penetration formulation. Unfortunately, this is a fairly complex task and no attempt was made to implement it during this program. However, if one assumes that the depth of penetration is more strongly dependent on particle size than on velocity, certain information can be obtained by inspection. For example, Fig. 24 is a histogram of particle radii obtained using the X-Y plotter. Figure 16, above, is a histogram of crater diameters which was obtained from a gold target bombarded by particles with a size distribution as shown in Fig. 24. It is fairly safe to assume that the average crater was produced by the average particle. This implies that the crater diameter to particle diameter ratio is about 3.5 for a gold target at about 5 km/sec. Similar estimates for a stainless steel target gives a value of two or less.

Although these measurements are by no means definitive, the values were used for extrapolation purposes in the following section. It is felt that this technique, with certain refinements, could provide valuable information on hypervelocity cratering by small particles.

For true hypervelocity impact, the cratering process is relatively insensitive to particle shape providing the particles are not long cylinders or rods. As suggested earlier, the particles used in this work are assumed to be spherical and all calculations have been based on this assumption. Evidence

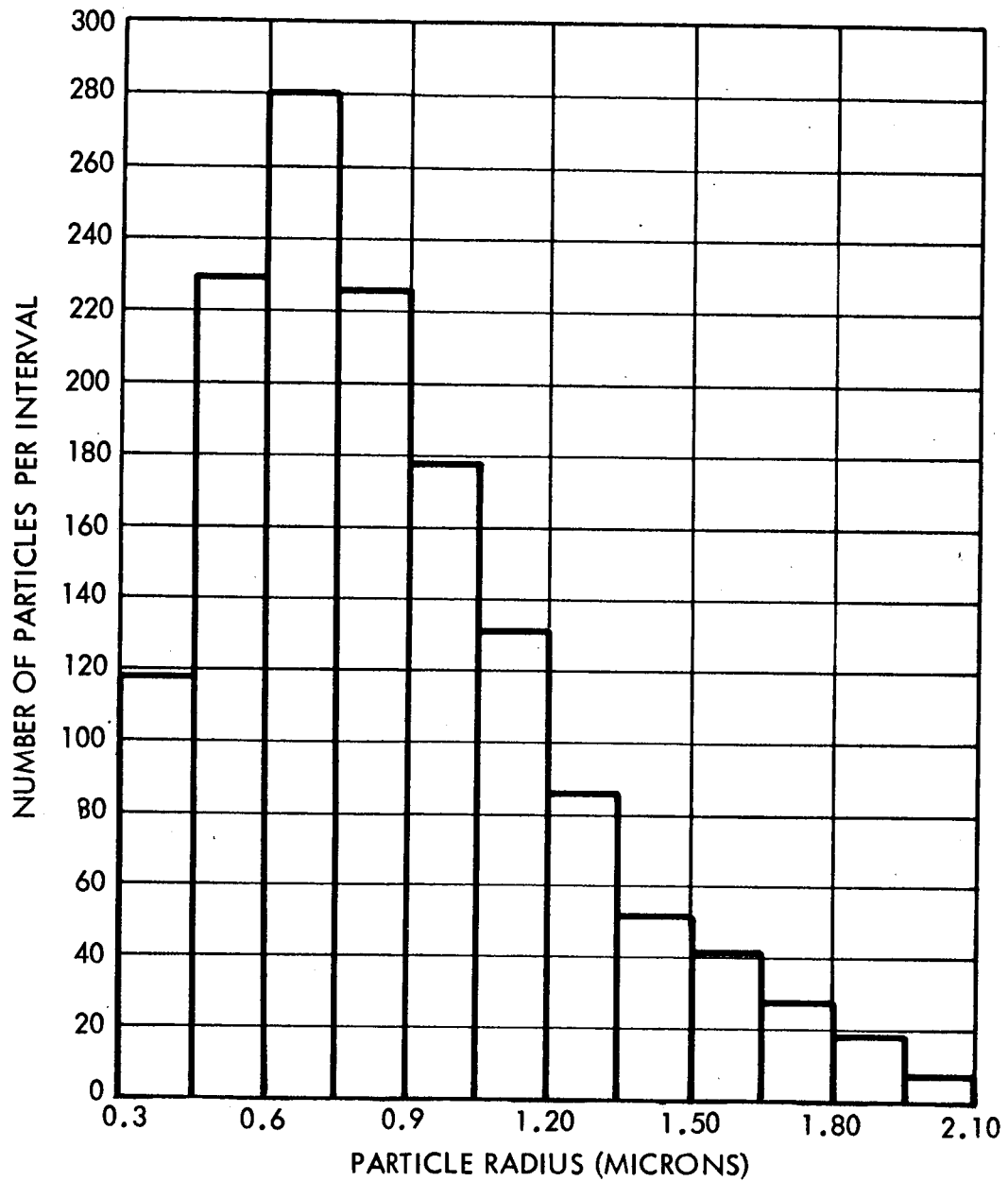


Figure 24. Histogram of Particle Radii. The data were obtained with the electronic X-Y plotter over several different runs.

for this assumption is illustrated in Fig. 25 which is an electron micrograph (magnification 30,000X) of some of the iron particles. Departure from sphericity is obviously quite small.

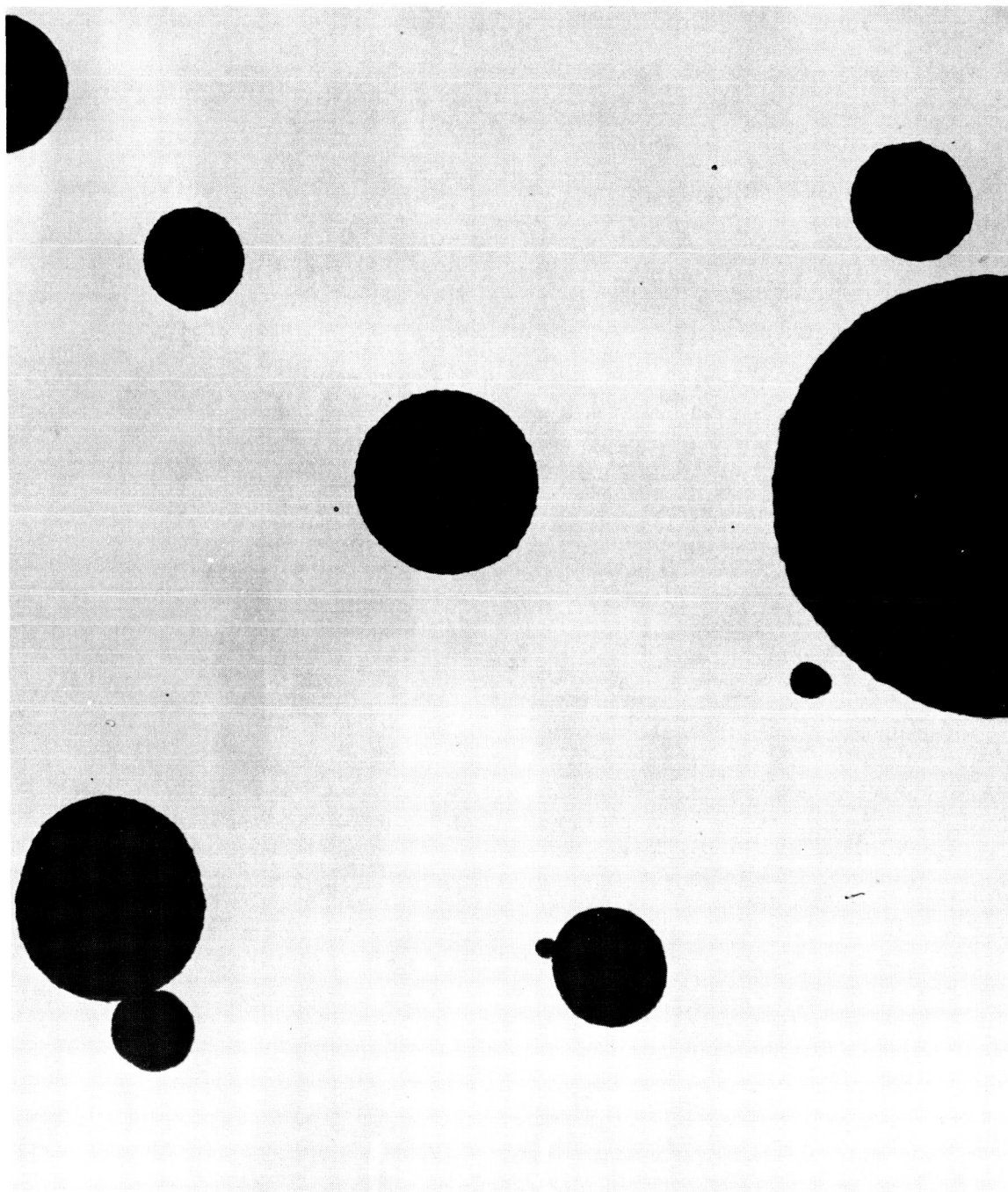


Figure 25. Electron Micrograph of the Iron Particles.
(Magnification 30,000X). The scale divisions
correspond to one micron.

IV. DISCUSSION OF RESULTS

It is not evident from the results presented above that micrometeoroid bombardment of thermal control surfaces presents a major hazard. Up to 30% surface damage is required to change the emissivity of highly reflecting surfaces by a significant amount. In terms of numbers of particles required to inflict this degree of damage, the laboratory exposure is equivalent to several years in space. However, it must be recognized that the laboratory results alone are not sufficient to predict the behavior of metals in the space environment because the effects are strongly dependent upon the meteoritic flux and the properties of individual meteoroids. Extrapolation of the test results is, at best, a speculative procedure. However, the brief exercise outlined in the following paragraphs, tends to identify the major problem areas and provides a framework for the examination of the test results.

The objective of the exercise is to estimate the space exposure simulated by the experimental results. For the sake of simplicity, we limit the discussion to a single target material; namely, gold. From the results above, we see that the average crater diameter to particle diameter ratio (D_c/d) is about 3.5 for iron particles. This is obtained for a mean velocity of about 5 km/sec. The mean micrometeoroid velocity is usually taken as 30 km/sec. Assuming that the depth of penetration increases as the ratio of velocities to the two-thirds power, D_c/d at 30 km/sec would be about 12.

Another factor which effects D_c/d is the particle density. All of the experimental work was done with iron particles having a density of about 8 gms/cm³. There is reason to suspect that micrometeoroids are composed of lower density material. A density of 2 gms/cm³ was chosen

arbitrarily for purposes of evaluation. Although we have no direct experimental measurements on the relative cratering efficiencies of different density particles, a value of $D_c/d = 2$ at 5 km/sec appears to be a conservative estimate. By the same arguments used above, D_c/d would be about 6.6 at 30 km/sec.

The meteoroid flux is usually expressed as a cumulative mass distribution curve. The one suggested by Alexander, et al,⁸ which is based on the results of direct satellite measurements, will be used. Their curve gives the flux of meteoroids with mass greater than a specified value. Using this curve and the cratering criteria from above, some simplified calculations on anticipated crater coverage for a gold target have been made. The results of these calculations are shown in Table III for particles of densities 8 gm/cm^3 and 2 gm/cm^3 .

First, meteoroid mass was specified and the flux corresponding to that value was determined from Alexander's curve. Assuming spherical particles, the diameters of particles corresponding to the specified mass were determined. The crater diameter and area were calculated based on the assumptions described above. Finally, the fraction of unit area covered by craters was computed and is given in the last column.

Implicit in these calculations is the fact that for a given mass all particles are identical which is an oversimplification and yields a lower value of coverage. More properly, the total coverage should be computed analytically from a differential flux representation. Nevertheless, the magnitude of anticipated coverage is similar to the coverage obtained in the laboratory experiments. Therefore, we conclude that the experiments simulate about one year's exposure to the space environment, or less.

TABLE III
CALCULATED CRATER COVERAGE FOR NATURAL METEORIODS*

Meteoroid Mass (kg)	Flux (Particles/m ² /sec)	Meteoroid Density (gm/cm ³)	Particle Diameter (Microns)	Crater Diameter (Microns)	Crater Area (Microns ²)	Coverage (%/Year)
10 ⁻¹⁷	200	8	0.14	0.8	0.5	0.3
10 ⁻¹⁵	100	8	0.6	3.7	10.9	3.2
10 ⁻¹⁴	10	8	1.4	8.2	52.5	1.7
10 ⁻¹³	1	8	2.9	17.4	237.0	0.8
10 ⁻¹⁶	150	2	0.5	3.3	8.5	4.0
10 ⁻¹⁵	100	2	1.0	6.6	34.2	10.8
10 ⁻¹⁴	10	2	2.1	13.8	150.0	4.7
10 ⁻¹³	1	2	4.5	29.7	690.0	2.2

*Calculations based on the cratering measurements using iron particles on gold targets.
See text for extrapolation procedure employed.

Perhaps the most obvious conclusion which can be reached from these measurements is that the thermal radiation properties of certain classes of materials are much less susceptible to change than others. Generally, materials which resist hypervelocity penetration exhibit smaller changes. For example, stainless steel targets require roughly three times as many impacts as gold targets to give comparable changes in emittance. Vapor deposited aluminum on a resin substrate indicated the smallest change of all the materials examined. This is attributed to the peculiar cratering mechanism exhibited by this type of target. Apparently the craters are quite deep relative to their diameter. Since changes in emissivity appear to be related to the surface area affected, this type of material suffers little change.

A factor which has not been examined is the effect of mean crater size. For gold targets, the average crater diameter obtained in the laboratory was about 5 to 6 microns. It is apparent from Table III that significant coverage is represented by craters of widely different sizes. The effect of crater size on radiation properties would provide another valuable piece of information to support extrapolation procedures.

V. SUMMARY

The experimental program, described above, has shown that micrometeoroid damage to thermal control materials can be simulated in the laboratory. The effects, although not serious in most cases, are significant and should be considered in the knowledgeable design of spacecraft thermal control systems.

REFERENCES

1. Friichtenicht, J. F., Rev. of Sci. Inst., Vol. 33, 209 (1962).
2. Shelton, H., Hendricks Jr., C. D., and Wuerker, R. F., J. Appl. Phys., Vol. 31, 1243 (1960).
3. Edwards, D. K., Gier, J. T., Nelson, K. E., and Roddick, R. D., "Integrating Sphere for Imperfectly Diffuse Samples", JOSA 51:1279-1288 (1961).
4. Dunkle, R. V., Edwards, D. K., Gier, J. T., Nelson, K. E., and Roddick, R. D., "Heated Cavity Reflectometer for Angular Measurements", Progress in International Research on Thermodynamic and Transport Properties, ASME 541-562 (1962).
5. Dunkle, R. V., "Research in Heat Transfer", Adlard and Son Ltd., Dorking, Surrey, England, (1963).
6. Schmidt, E., and Eckert, E., "Über die Richtungsverteilung der Wärmestrahlung von Oberflächen", Forsch. Gebiete Ingenieurw, 6:175-183 (1935).
7. McNicholas, H. J., "Absolute Methods of Reflectometry", National Bureau of Standards Journal of Research, 1:20 (1928).
8. Alexander, McCracken, Secretan and Berg, "Review of Direct Measurements of Interplanetary Dust from Satellites and Probes", Paper presented to the COSPAR Meeting, (May 1962).